e-ISSN 2150-5551
CN 31-2103/TB

Nano-Micro Letters

REVIEW

https://doi.org/10.1007/s40820-022-00901-w

Cite as
Nano-Micro Lett.
(2022) 14: 178

Received: 15 May 2022
Accepted: 26 June 2022

Recent Advancements on Photothermal Conversion and Antibacterial Applications over MXenes-Based Materials

Shuyan Hao[1], Hecheng Han[1], Zhengyi Yang[1], Mengting Chen[2], Yanyan Jiang[1,3] ✉, Guixia Lu[4], Lun Dong[5] ✉, Hongling Wen[2], Hui Li[1], Jiurong Liu[1] ✉, Lili Wu[1], Zhou Wang[1], Fenglong Wang[1,3] ✉

HIGHLIGHTS

- Fabrication, characterizations and photothermal properties of MXenes are systematically described.
- Photothermal-derived antibacterial performances and mechanisms of MXenes-based materials are summarized and reviewed.
- Recent advances in the derivative applications relying on antibacterial properties of MXenes-based materials, including in vitro and in vivo sterilization, solar water evaporation and purification, and flexible antibacterial fabrics, are investigated.

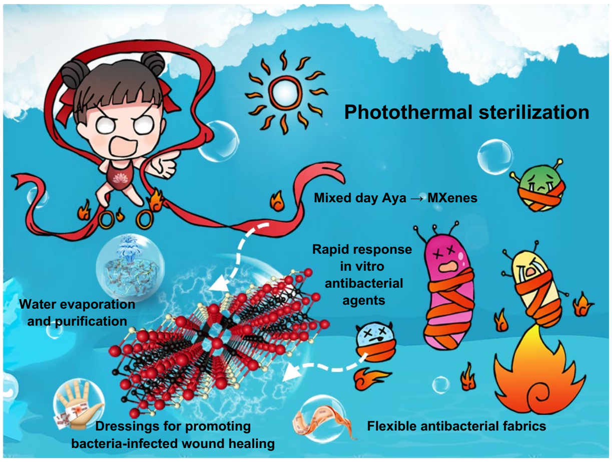

ABSTRACT The pernicious bacterial proliferation and emergence of super-resistant bacteria have already posed a great threat to public health, which drives researchers to develop antibiotic-free strategies to eradicate these fierce microbes. Although enormous achievements have already been achieved, it remains an arduous challenge to realize efficient sterilization to cut off the drug resistance generation. Recently, photothermal therapy (PTT) has emerged as a promising solution to efficiently damage the integrity of pathogenic bacteria based on hyperthermia beyond their tolerance. Until now, numerous photothermal agents have been studied for antimicrobial PTT. Among them, MXenes (a type of two-dimensional transition metal carbides or nitrides) are extensively investigated as one of the most promising candidates due to their high aspect ratio, atomic-thin thickness, excellent photothermal performance, low cytotoxicity, and ultrahigh dispersibility in aqueous systems. Besides, the enormous application scenarios using their antibacterial properties can be tailored via elaborated designs of MXenes-based materials. In this review, the synthetic approaches and textural properties of MXenes have been systematically presented first, and then the photothermal properties and sterilization mechanisms using MXenes-based materials are documented. Subsequently, recent progress in diverse fields making use of the photothermal and antibacterial performances of MXenes-based materials are well summarized to reveal the potential applications of these materials for various purposes, including in vitro and in vivo sterilization,

---

✉ Yanyan Jiang, yanyan.jiang@sdu.edu.cn; Lun Dong, dlunregister@163.com; Jiurong Liu, jrliu@sdu.edu.cn; Fenglong Wang, fenglong.wang@sdu.edu.cn
[1] Key Laboratory for Liquid-Solid Structural Evolution and Processing of Materials Ministry of Education, Shandong University, Jinan 250061, People's Republic of China
[2] Department of Virology, School of Public Health, Shandong University, Jinan 250012, People's Republic of China
[3] Shenzhen Research Institute of Shandong University, A301 Virtual University Park in South District of Nanshan High-Tech Zone, Shenzhen 518057, People's Republic of China
[4] School of Civil Engineering, Qingdao University of Technology, Qingdao 266033, People's Republic of China
[5] Department of Breast Surgery, Qilu Hospital, Shandong University, Jinan 250012, People's Republic of China

solar water evaporation and purification, and flexible antibacterial fabrics. Last but not least, the current challenges and future perspectives are discussed to provide theoretical guidance for the fabrication of efficient antimicrobial systems using MXenes.

KEYWORDS MXenes; Antibacterial mechanisms; Photothermal properties; Antibacterial applications

1 Introduction

As a global problem, uncontrollable harmful bacterial proliferation has posed great threat to public health, which eventually caused economic burdens to the infected patients and the whole society [1, 2]. The infectious bacteria always brought in wound infections [3, 4], disease transmission [5, 6], water contamination [7], soil contamination [8], and widespread corrosions [9]. From a traditional viewpoint, antibiotics have held the top priority in the eradication of bacterial growth. Nevertheless, the emergence of antibiotic-resistant pathogens due to antibiotic abuse results in the failure of antibiotic therapy, becoming one of the most significant global challenges [10]. The drug-resistant bacteria have developed penetration barriers, drug efflux pumps, inactivating enzymes to protect themselves from the developed antibiotics [11, 12]. In addition, bacteria could also shelter from the attack of drugs or harsh conditions by forming the biofilm, a structure that serves as a sanctuary of the inner cells [13, 14]. Besides, horizontal gene transfer can disseminate resistance genes among biofilm wrapped bacteria, amplifying the bacterial resistance [15]. Unquestionably, the emergence of drug-resistant bacterial and the formation of biofilms leads to the dreadful biological crisis. Thus, searching for novel efficient treatment approaches without inducing drug resistance is of great significance for solving these issues. Recently, non-invasive photothermal therapy (PTT) functioning under light irradiation represents a promising alternative to antibiotics in the fight against bacterial proliferation [16, 17]. Based on hyperthermia beyond tolerance, this kind of therapy could efficiently damage the integrity of pathogenic bacteria in a controllable manner [18]. Furthermore, bacteria were unlikely to develop resistance to PTT as they did to antibiotics by drug excretion, facilitating metabolism and postponing absorption [11, 19]. In the PTT process, hyperthermia originating from the photo-to-thermal conversion process on the PTT agents could cause protein denaturation and inactivation, deoxyribonucleic acid (DNA) cross-linking and cell membrane loosening, which also facilitates the penetration of other available antibacterial agents to destroy the biofilm structure [20]. These satisfactory properties of PTT exhibit the feasibilities of using antibiotics-independent techniques to destroy harmful bacteria, thereby attracting extensive attention. To achieve desirable antibacterial efficiency and less light energy consumption, synergistic tactics by combining PTT with other techniques, such as photodynamic therapy (PDT) and metal ions incursion, have been brought into focus [21–23]. The heat generated by PTT could tremendously enhance the permeability of the bacteria membranes and promote the intracellular permeation of reactive oxygen species (ROS) or metal ions [24]. These synergistic tactics could not only lower the dosage requirements of photothermal agents, but also offset the imperfections of other therapies. In the post-antibiotic era, their high therapeutic efficiency has been proved, and it is considered safer and more thriving representatives in the field of antibacterial applications [21, 25, 26].

Various photothermal materials have been exploited and designed, such as carbon-based materials [27], noble metal nanoparticles [28], conjugated polymers [29], and metal–organic frameworks [30]. Among these candidates, MXenes have stood out due to the high aspect ratio, atomic-thin thickness, excellent photothermal performance, low toxicity, and ultrahigh dispersibility in aqueous systems [31–34]. MXenes represent a large group of two-dimensional (2D) transition metal carbides, carbonitrides, and nitrides with the general chemical formula $M_{n+1}X_nT_x$ [33]. In this chemical formula, M represents early transition metals like Ti, Mn, V, Nb, Mo, Sc, Cr, etc., X stands for C and/or N, T_x means surface-terminating functional groups (mainly OH, O, and F), and n ranges from 1 to 5 [35]. This group of 2D materials exhibits strong light absorption performances of covering the entire ultraviolet (UV), visible, and near-infrared (NIR) ranges, showing great potential in photo energy conversion [36]. MXenes can directly act as PTAs or photosensitizers (PSs) by using photo-responsive building units, due to their intrinsic photothermal and photodynamic abilities [37, 38]. They can also achieve photo-induced medicinal ability by loading antibacterial agents or forming zero-dimensional (0D)/2D structures, one-dimensional (1D)/2D structures, and other

https://doi.org/10.1007/s40820-022-00901-w

architectures [39, 40]. Profoundly, the appropriate design and modification of MXenes could tune their light absorption performances [41], postpone the recombination of electrons and holes for promoting ROS generation [25], and improve the unique localized surface plasmonic resonance (LSPR) effect for enhanced photo-to-thermal conversion [42]. MXenes with low cytotoxicity and high biocompatibility are also excellent platforms for in vivo therapy, such as bacterial infection treatment, re-epithelialization acceleration, and granulation tissue formation, which vastly ameliorates the therapeutic efficacy with respect to traditional bandages [22, 27]. Moreover, profiting from their desired merits, including hydrophilicity, high aspect ratio morphology, and metallic conductivity, when MXenes are incorporated into thin film or hydrogel systems, they offer versatile potentials to design MXenes-based antibacterial soft materials with tunable properties [43, 44]. They also possess superb mechanical stability and solution processability, suitable for further assembly into various geometry and textile structures, thus realizing the concept of the recent trend in flexible and wearable electronic textiles for innovative antimicrobial applications [45, 46].

Vast amounts of research work have been dedicated in the past decade to designing MXenes-based antimicrobial materials displaying physical puncture, photothermal therapy and photothermal-derived therapy properties [28, 47, 48]. However, by searching the literature database, there have been no systematic review study summarizing the antimicrobial properties of photo-induced mechanisms, as well as research progress in photothermal antibacterial related applications. Herein, in this review, we firstly make a systematic summary and introduction to the synthetic process and textural properties of MXenes. Next, we comprehensively summarize and analyze the antibacterial mechanisms, mainly involving their inherent photo-to-thermal properties, photothermal therapy, and other photo-induced synergistic therapies. Based on these, current advances in their photothermal dominated sterilization are emphatically introduced, including rapid response in vitro antibacterial agents, dressings for promoting bacteria-infected wound healing, solar-driven water evaporation and purification, and flexible antibacterial fabrics (Fig. 1). Finally, we prospect the opportunities and challenges faced by MXenes-based materials for antibacterial applications in future.

2 Synthesis and Microstructure of MXenes

MXenes, as a new family of 2D materials, have attracted research booms and achieved continuous progress since they came into sight. Here forward-looking summaries of the synthetic methodology and microstructure characterizations are presented. Comprehensive understandings of the preparation process and microstructure will deepen the fundamental knowledge of the properties of MXenes, which could enable their applications with ingenious contraptions in diverse emerging fields.

2.1 Synthesis of MXenes

2.1.1 Approaches for Preparation of MXenes

The MAX phase ($M_{n+1}AX_n$) is the precursor for the preparation of MXenes, in which the bonding between M and X shows the mixed characteristics of covalent bonds, metal bonds and ionic bonds, while the bonding between M and A exhibits the characteristics of metal bonds [49]. It can be seen that unlike graphene or molybdenum disulfide, in which the layers are combined through van der Waals forces, the MAX phase is more difficult to be exfoliated, and thus more corrosive agents are necessary [50]. For a typical synthetic approach, the preparation of MXenes proceeds in two steps, which are the selective etching of the A-layer atoms (e.g., Al, Si, Ga) from the corresponding MAX phase and the subsequent delamination of multilayered MXenes (Fig. 2a) [35]. After wet chemical etching, loosely stacked MX layers are obtained and can be further separated into single-layered flakes. Hydrofluoric acid (HF), as the etchant, was firstly employed to effectively eradicate the A layers from the MAX phase and generated OH and F surface terminated groups [51]. In a pioneering work, Naguib et al. [51] immersed the MAX phased powder in a 50 wt% hydrofluoric acid solution at room temperature and then washed the obtained suspension with deionized water. After etching and centrifugation, the original compact packing structure was converted into a slack accordion-like architecture, as shown in Fig. 2b, c. The following simplified reaction formula could describe the above process for selective removal of A layers from the MAX phase:

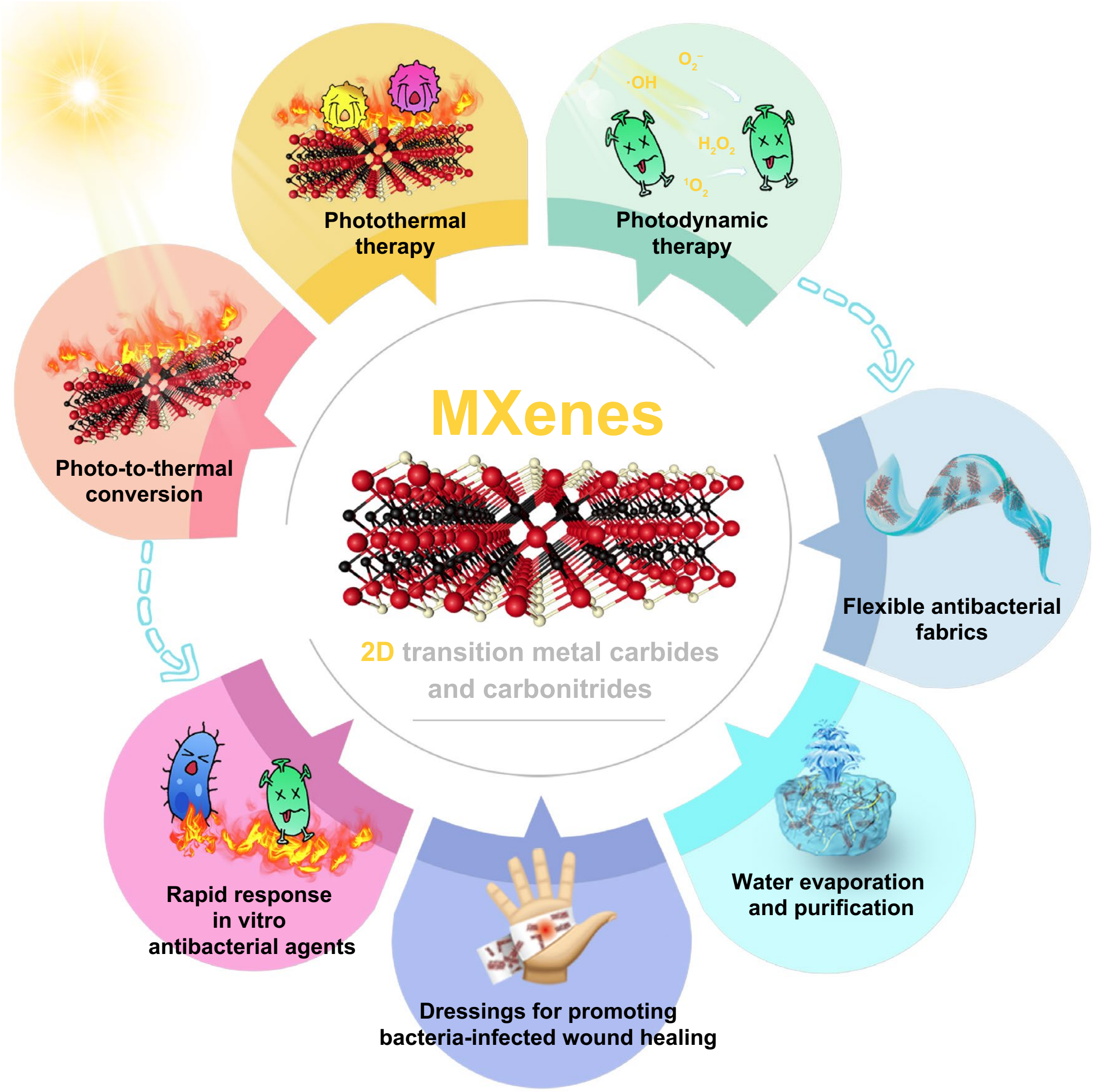

Fig. 1 The effective photothermal antibacterial performances of MXenes endow them with widespread application potential

$$Ti_3AlC_2 + 3HF \rightarrow AlF_3 + \frac{3}{2}H_2 + Ti_3C_2 \quad (1)$$

$$Ti_3C_2 + 2H_2O \rightarrow Ti_3C_2(OH)_2 + H_2 \quad (2)$$

$$Ti_3C_2 + 2HF \rightarrow Ti_3C_2F_2 + H_2 \quad (3)$$

As a widely adopted method, hydrofluoric acid etching is effective for the rapid etching of the MAX phase. However, it cannot be ignored that HF solutions are highly corrosive, harmful and prone to cause over-etching [52]. Hence, in later stage, new etching systems such as HCl/LiF [53], NH_4HF_2 [54], and NH_4F [55] have been employed to pursue mild etching conditions, which greatly enriched the synthetic approaches of MXenes. Incorporating cations (such as Li^+, Na^+, and Sn^{4+}) between the $M_{n+1}X_n$ layers could lead to the expansion of the interlayer separations and the weakening of interlayer connections [56–60]. Therefore, MXenes nanosheets exhibit fewer defects, larger sizes, and more uniform thicknesses. For instance, Ghidiu et al. [61] added 1.98 g of LiF to 6 M HCl to etch Ti_3AlC_2 powders and successfully fabricated clay-like MXenes with excellent

https://doi.org/10.1007/s40820-022-00901-w

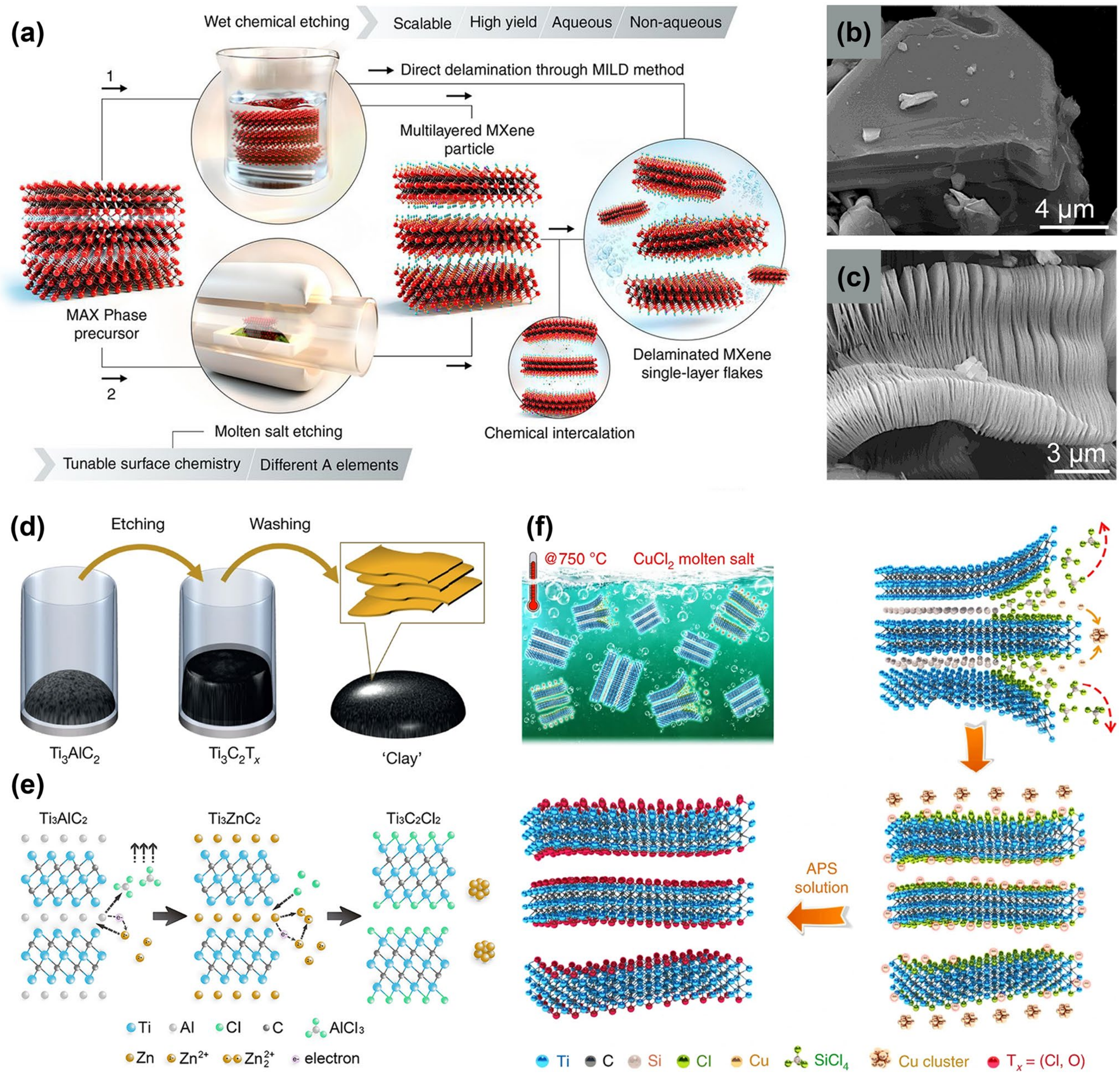

Fig. 2 **a** Schematic illustration of two approaches to produce MXenes by removal of A layers from MAX phases and related layered compounds [35]. Copyright 2021, The American Association for the Advancement of Science. **b** SEM image of Ti_3AlC_2 particle before HF treatment; **c** SEM image of Ti_3AlC_2 particle after HF treatment [72]. Copyright 2012, American Chemical Society. **d** Schematic of clay-like MXenes etched by HCl and LiF [61]. Copyright 2014, Springer Nature. **e** Schematic of MXenes etched by molten $ZnCl_2$ [66]. Copyright 2019, American Chemical Society. **f** Schematic of MXenes etched by molten $CuCl_2$ [67]. Copyright 2020, Springer Nature

dispersibility and hydrophilicity (Fig. 2d). After being dried, the resulted hydrophilic materials could be shaped like clay and rolled into a thin film with thickness of a few micrometers. In addition to etching the common Ti_3AlC_2, Du et al. [59] found that after treating the Ti_3AlCN MAX phase with the mixture of LiF and HCl, a uniform Ti_3CNT_x colloidal solution could be obtained by ultrasonic and hand-shaking. With a "fluffy" morphology and a relatively small percentage of nanosheets, the Ti_3CNT_x powder exhibited excellent charge storage and handling capabilities as well as excellent cycling properties. Apart from LiF/HCl system, NH_4HF_2 could also be used as an etchant by inserting the cation NH^{4+} in the accordion-like MXenes [62]. The etching process can be clearly illustrated in the following simplified reaction formula [63]. In particular, instead of AlF_3, $(NH_4)_3AlF_6$ as the product was produced, and among the layers of $Ti_3C_2T_x$, NH_3 and NH^{4+} were intercalated. In addition to the above procedures, researchers have also successfully synthesized MXenes through the reaction of other fluoride salts such as NaF and KF with hydrochloric acid [64, 65].

$$Ti_3AlC_2 + 3NH_4HF_2 \rightarrow \left(NH_4\right)_3AlF_6 + Ti_3C_2 + \frac{3}{2}H_2 \tag{4}$$

$$Ti_3C_2 + aNH_4HF_2 + 2H_2O \rightarrow \left(NH_3\right)_c\left(NH_4\right)_dTi_3C_2(OH)_xF_y \tag{5}$$

Beyond that, current advances have demonstrated that MXenes could also be acquired through the relatively mild molten salt etching procedures without using the fluorine-containing materials [32]. One of them is the Lewis acid molten salt stripping method, which is much safer compared with the etching process. Li et al. [66] demonstrated that the MAX phase (Ti_3AlC_2) and molten $ZnCl_2$ salt would react violently under specific conditions. In the reaction system, Zn^{2+} ions played a similar role as the hydrogen ion in HF, while Cl^- instead of F^- coordinated with M (Fig. 2e). As a result of the replacement process between the Zn element from molten $ZnCl_2$ and the A-site element in MAX phase precursors (Ti_3AlC_2, Ti_2AlN, and V_2AlC), not only a series of new $M_{n+1}ZnX_n$ phases (Ti_3ZnC_2, Ti_2ZnC, Ti_2ZnN, and V_2ZnC) were obtained, but also the MXenes with Cl-terminated functional groups ($M_{n+1}X_nCl_2$) were generated. Moreover, Li et al. [67] successfully extended the stripping strategy to a variety of Lewis acid chloride molten salts (such as $CuCl_2$, $ZnCl_2$, $FeCl_2$, and AgCl) and broader MAX phase family members (such as the A-site element is Si, Al, Zn, and Ga). Figure 2f is the schematic illustration of $Ti_3C_2T_x$ MXenes prepared by Ti_3SiC_2 MAX phase and $CuCl_2$ Lewis molten salt. This study demonstrated that Cu^{2+} in molten salt could feasibly oxidize Si to Si^{4+} at 750 °C. Si^{4+} eventually formed $SiCl_4$ with Cl^- and escaped from the Ti_3C_2 sublayer, while Cu^{2+} was reduced to Cu metal. The residual Cu species in the products could be removed using ammonium sulfate solution, and finally, $Ti_3C_2T_x$ MXenes was obtained. In contrast with conventional etching methods, Lewis acid molten salt stripping process could proceed in a much more convenient and safer manner.

Besides the aforementioned top-down approaches through chemical etching and molten salt stripping methods, chemical vapor deposition (CVD) was recently studied as a bottom-up technique for the synthesis of MXenes. As compared to the top-down etching process, the material synthesized by CVD exhibits high crystalline feature [68]. The first demonstration of large-area ultrathin transition metal carbides (TMCs) through the CVD method was reported by Xu et al. [68]. In this study, methane was used as the carbon source, and Cu foil sat on a Mo foil as the substrate. At temperature higher than 1085 °C, high-quality 2D ultrathin TMCs crystals with a thickness of a few nanometers and a lateral dimension exceeding 100 μm were grown. Subsequently, Geng et al. [69] further extended this method to synthesize a high-quality and uniform Mo_2C film from the initial micrometer range to the centimeter range on graphene. They also confirmed that graphene-templated growth of Mo_2C exhibits a single crystal structure with a larger size and lower defect density. Compared with the MXenes obtained from etching methods, minor defects and no terminations in the CVD generated MXenes, open a new door for investigating their intrinsic properties and domain boundaries effect [70]. However, the structure generated by CVD is typically a thin film rather than a single layer, which is unsatisfied with the demands of mainstream applications, and thus more work should be done to achieve the CVD-produced single-layered MXenes in the future [71].

Table 1 summarizes the etching parameters of typical methods, including the etching method, MAX phases and their corresponding attainable MXenes, etchants, etching temperature, and etching time.

2.1.2 Delamination of MXenes

For the etched multilayered MXenes, delaminating them into 2D flakes with a few or even single layers is vital for better dispersibility, photothermal conversion ability, and high reactivity [78, 79]. 2D materials have long occupied an important status in photothermal conversion due to their robust dispersibility and facile surface functionalization [80]. When 2D nanomaterials come into service, their thickness is an essential factor affecting their photothermal properties. The thermal conductivity is also inclined to be higher for few-layered materials compared to multilayered materials [78]. Therefore, delamination (e.g., through sonication) is required to fabricate dispersed MXenes nanosheets, which increases the interlayer spacings and makes the layers exfoliated into the separated 2D feature [81]. It has been found that the use of intercalants can effectively facilitate the delamination of the multilayered MXenes. With the assistance of intercalants, the production of single/few-layered MXenes can be significantly increased by simple treatments such as handshaking, mechanical vibration and ultrasound sonication [49, 76]. For instance, by using tetramethylammonium hydroxide (TMAOH) as an intercalant, bulky TMA^+ cations could effectively access the gallery space and facilitate delamination [82]. The subsequent breakdown of the precursor layered crystals into separated elementary layers could be proceeded with the insertion of TMA^+ cations, as shown in Fig. 3a. In the obtained colloidal solution, the appearance is almost transparent, indicating multilayered MXenes were delaminated into extremely thin sheets (Fig. 3b, c). In the atomic force microscope (AFM) illustration, the height was estimated to be ca. 1.6–2.0 nm by line scanning across the plain area of the flakes (Fig. 3d). In this way, it was confirmed that in the colloidal solution, monolayer and bilayer nanosheets were dominated. Apart from TMAOH, Halim et al. [76] used tetrabutylammonium hydroxide (TBAOH) as the intercalant to delaminate Mo_2CT_x under sonication in an ice-cold ultrasonic bath for one hour, realizing the synthesis and delamination of 2D Mo_2CT_x (Fig. 3e). The XRD pattern showed that in the absence of TBAOH treatment, two peaks ascribed to (0002) facets appeared corresponding to c lattice parameters (c-LPs) of 21.2 and 26.9 Å, respectively (Fig. 3f). Upon intercalation with TBAOH, two (0002) peaks appeared corresponding to c-LPs of 28.5 and 58.1 Å, which means the intercalation of TBA^+ cations and water molecules.

Table 1 Summary of typical methods used for the preparation of MXenes

Methods	Precursor	Obtained MXenes	Etching conditions		References
			Etchants	Time and Temp.[a]	
HF etching	Ti_3AlC_2	$Ti_3C_2T_x$	HF (50 wt%)	2 h, RT[b]	[51]
	Ti_3SiC_2	$Ti_3C_2T_x$	HF (30 wt%), H_2O_2 (35 wt%)	45 h, 40 °C	[73]
	V_2AlC	V_2CT_x	HF (50 wt%)	90 h, RT[b]	[74]
	Nb_2AlC	Nb_2CT_x	HF (50 wt%)	90 h, RT[b]	[74]
	Ti_3AlCN	Ti_3CNT_x	HF (50 wt%)	18 h, RT[b]	[72]
	Mo_2TiAlC_2	$Mo_2TiC_2T_x$	HF (50 wt%)	90 h, 55 °C	[75]
	$Mo_2Ti_2AlC_3$	$Mo_2Ti_2C_3T_x$	HF (50 wt%)	48 h, RT[b]	[75]
	$Mo_2Ga_2C_2T_x$	Mo_2C	HF (50 wt%)	160 h, 55 °C	[76]
In situ HF formation etching	Ti_3AlC_2	$Ti_3C_2T_x$	HCl (6 M), LiF	45 h, 40 °C	[61]
	Ti_2AlC	Ti_2CT_x	HCl (12 M), NaF (4 M)	24 h, 60 °C	[55]
	Ti_3AlC_2	$Ti_3C_2T_x$	HCl (12 M), KF (4 M)	48 h, 40 °C	[55]
	Ti_3AlC_2	$Ti_3C_2T_x$	HCl (12 M), NH_4F (4 M)	48 h, 40 °C	[55]
	Ti_3AlC_2	$Ti_3C_2T_x$	HCl (12 M), NH_4F (4 M)	24 h, 30 °C	[55]
	Ti_3AlC_2	$Ti_3C_2T_x$	NH_4HF_2 (2 M)	24 h, RT[b]	[52]
	V_2AlC	V_2CT_x	HCl (12 M), NaF (2 g)	72 h, 90 °C	[77]
Lewis acid molten salt etching	Ti_3SiC_2	$Ti_3C_2T_x$	$CuCl_2$	24 h, 750 °C, Ar	[67]
	Ti_3ZnC_2	$Ti_3C_2T_x$	$FeCl_2$	24 h, 750 °C, Ar	[67]
	Ti_3ZnC_2	$Ti_3C_2T_x$	$CoCl_2$	24 h, 750 °C, Ar	[67]
	Ti_3ZnC_2	$Ti_3C_2T_x$	$NiCl_2$	24 h, 750 °C, Ar	[67]
	Ti_3ZnC_2	$Ti_3C_2T_x$	$CuCl_2$	24 h, 750 °C, Ar	[67]
	Ti_3ZnC_2	$Ti_3C_2T_x$	$AgCl_2$	24 h, 750 °C, Ar	[67]
	Ti_3ZnC_2	$Ti_3C_2T_x$	$CdCl_2$	24 h, 650 °C, Ar	[67]
	V_2AlC	V_2CT_x	$ZnCl_2$	5 h, 550 °C, Ar	[66]
	Ti_2AlC	Ti_2CT_x	$ZnCl_2$	5 h, 550 °C, Ar	[66]

[a] Temp.: temperature; [b] RT: room temperature

Many kinds of intercalants such as metal ions, organic molecules, and inorganic molecules have been used to delaminate the multilayered MXenes and increase the yield of single/few-layered MXenes [33, 82–84]. Due to the increasing application fields, MXenes nanosheets with high quality and low contents of defects are highly desired, and it is far-reaching to review the previous studies to select the proper experimental conditions properly. The selection of intercalants and the design of intercalation conditions significantly influence defect rate, particle size, specific surface area, surface properties, and yield [33, 52, 83]. Table 2 summarizes the intercalation conditions used for different precursors under various etching conditions.

2.2 Microstructure and Surface Properties of MXenes

The characteristic microstructure of MXenes determines their unique physical and chemical properties. Similar to its parent phase ($M_{n+1}AX_n$), MXenes with the general formula $M_{n+1}X_nT_x$ exhibit hexagonal close-packed crystal structure [33]. Here, the early transition metal atoms at the M site follow the hexagonal close-packed model, and the carbon or

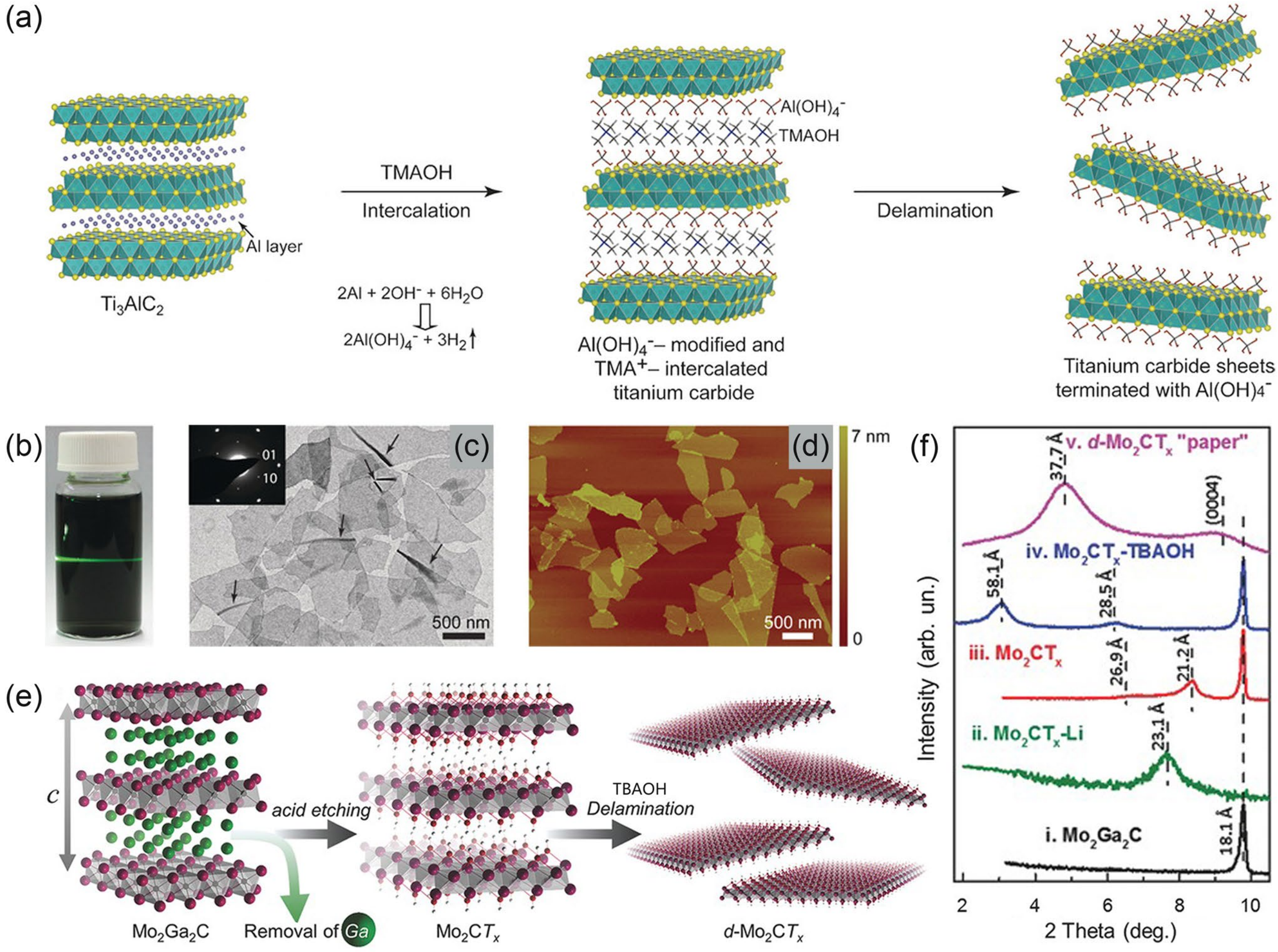

Fig. 3 **a** Schematic illustration of the intercalation and delamination process; **b** Photograph of the obtained nanosheet dispersion in H_2O with an apparent Tyndall effect; **c** Transmission electron microscopy (TEM) image of the extremely thin delaminated nanosheets; **d** AFM image of the extremely thin delaminated nanosheets [82]. Copyright 2016, Wiley–VCH. **e** Schematic illustration of the synthesis and delamination of Mo_2CT_x; **f** XRD patterns of Mo_2Ga_2C and Mo_2CT_x [76]. Copyright 2016, Wiley–VCH

nitrogen atoms at the X site fill the octahedral voids [33]. In MXenes, carbon and nitrogen atoms randomly fill octahedral voids, independent of carbonitride stoichiometry [92]. As shown in Fig. 4a, the M_2X, M_3X_2, M_4X_3, and M_5X_4 are the most common formula of the currently discovered MXenes [35]. In M_3C_2 and M_4C_3 materials, M atoms follow the face-centered cubic packing structure, but in the M_2X structure, the M atoms adopt the hexagonal close packing modes. The recently obtained M_5C_4 further enriched the diversity of the structure and expanded the theoretical number of MXenes to more than 100 [35]. At the microscopic level, the delaminated MXenes exhibit a typical lamellar structure. This morphology can be revealed by AFM micrographs (Fig. 4b) [93]. The layer spacing of MXenes has been experimentally verified to be 1 to 1.5 nm, and these values are wider than the reported graphene and phosphorene [61, 94, 95]. Furthermore, the hexagonal lattice structure in the axis zone along the c direction can be demonstrated from the high-resolution transmission electron microscopy (HRTEM) images, and the selected area electron diffraction (SAED) image confirmed the six-fold reflexes of lattice (Fig. 4c) [93].

Depending on the synthetic method used and the composition of MXenes, the surface of MXenes is covered with various terminations (Fig. 4d) [35]. Terminations are represented by T_x, which can be O, OH, NH, F, Cl, Br, S, Se, Te [92, 96]. The reaction in fluorine- and chlorine-containing solutions results in MXenes with mixed surface terminations, whose composition can be expressed as $(OH)_mO_xF_yCl_z$ [97–99]. Through thermal treatment and vacuum calcination, the terminations of MXenes can be modified in composition and coordination [100, 101]. For example, at temperatures above 775 °C, the terminations of $Ti_3C_2T_x$ can be completely defluorinated [100]. Surface terminations are intractable to avoid in experiments, so understanding them is essential. As shown in Fig. 4e, previous work by Zhou et al. [102] probed the orientations of OH and F in $Ti_3C_2X_2$. In type I, all F or OH groups are positioned above the hollow sites between three adjacent carbon atoms or point directly at the Ti atoms. For type II, all F or OH groups are found above the topmost C atoms on both sides of the main layer. The type III structure is a combination of types I and II, resulting in an asymmetrical arrangement on both sides of the main layer. In $Ti_3C_2X_2$ configurations, the structural stability can be assessed by comparing their relative total energies. Among $Ti_3C_2F_2$ and $Ti_3C_2(OH)_2$, type I conformer is most favorable in energy. Even so, for these three types, structural relaxations of their monolayers maintain the original geometrical integrity. The functionalized MXenes are also thermodynamically stable as the Gibbs energy change required for their formation is negative [103]. Additionally, the modification of surface functional groups exhibits a promising design space through chemical modifications. For example, the Cl and Br groups on MXenes can be replaced by O, S, Se, and Te, creating unique structural and electronic properties [96].

Table 2 Summary of intercalation conditions used for the preparation of MXenes through etching methods

Precursor	Obtained MXenes	Etching conditions		Intercalation conditions	References
		Etchants	Time and Temp.^{a}		
Ti_3AlC_2	$Ti_3C_2T_x$	HCl (6 M), LiF	45 h, 40 °C	Sonication, 1 h	[61]
Ti_3AlC_2	$Ti_3C_2T_x$	HF (50 wt%)	18 h, RT^b	Dimethyl sulfoxide, 18 h, RT; Sonication, 4 h	[85]
Ti_3AlC_2	$Ti_3C_2T_x$	HCl (37.2 wt%), LiF	24 h, 35 °C	TBAOH, 2 h	[86]
Ti_3AlC_2	$Ti_3C_2T_x$	HF (50 wt%)	22 h, RT	Dimethyl sulfoxide, 18 h, RT; Sonication, 6 h	[83]
Ti_3AlC_2	$Ti_3C_2T_x$	HF (50 wt%)	18 h, RT	$N_2H_4 \cdot H_2O$, 24 h, RT	[87]
Ti_3AlC_2	$Ti_3C_2T_x$	HF (40 wt%)	4 h, 40 °C	NaOH, 2 h, RT	[88]
Ti_3AlC_2	$Ti_3C_2T_x$	HF (0.1 g mL^{-1})	0.5 h, RT	TMAOH, Handshaking, 2 min, RT	[82]
Ti_3AlC_2	$Ti_3C_2T_x$	HF (49 wt%)	20 h, 60 °C	Sonication, 5 h	[89]
Ti_3AlC_2	$Ti_3C_2T_x$	HCl (9 M), LiF	24 h, 35 °C	Sonication, 1 h	[90]
Ti_2AlC	Ti_2CT_x	HF (10 wt%)	10 h, ice bath	Dimethyl sulfoxide, 18 h, RT; Sonication, 4 h	[91]
Mo_2Ga_2C	Mo_2CT_x	HF (14 M)	160 h, 55 °C	TBAOH, 18 h, RT	[76]
V_2AlC	V_2CT_x	HF (48 wt%)	92 h, RT	TBAOH, $(C_4H_9)_4NOH$, 2–21 h, RT	[84]

^{a}Temp.: temperature; ^{b}RT: room temperature

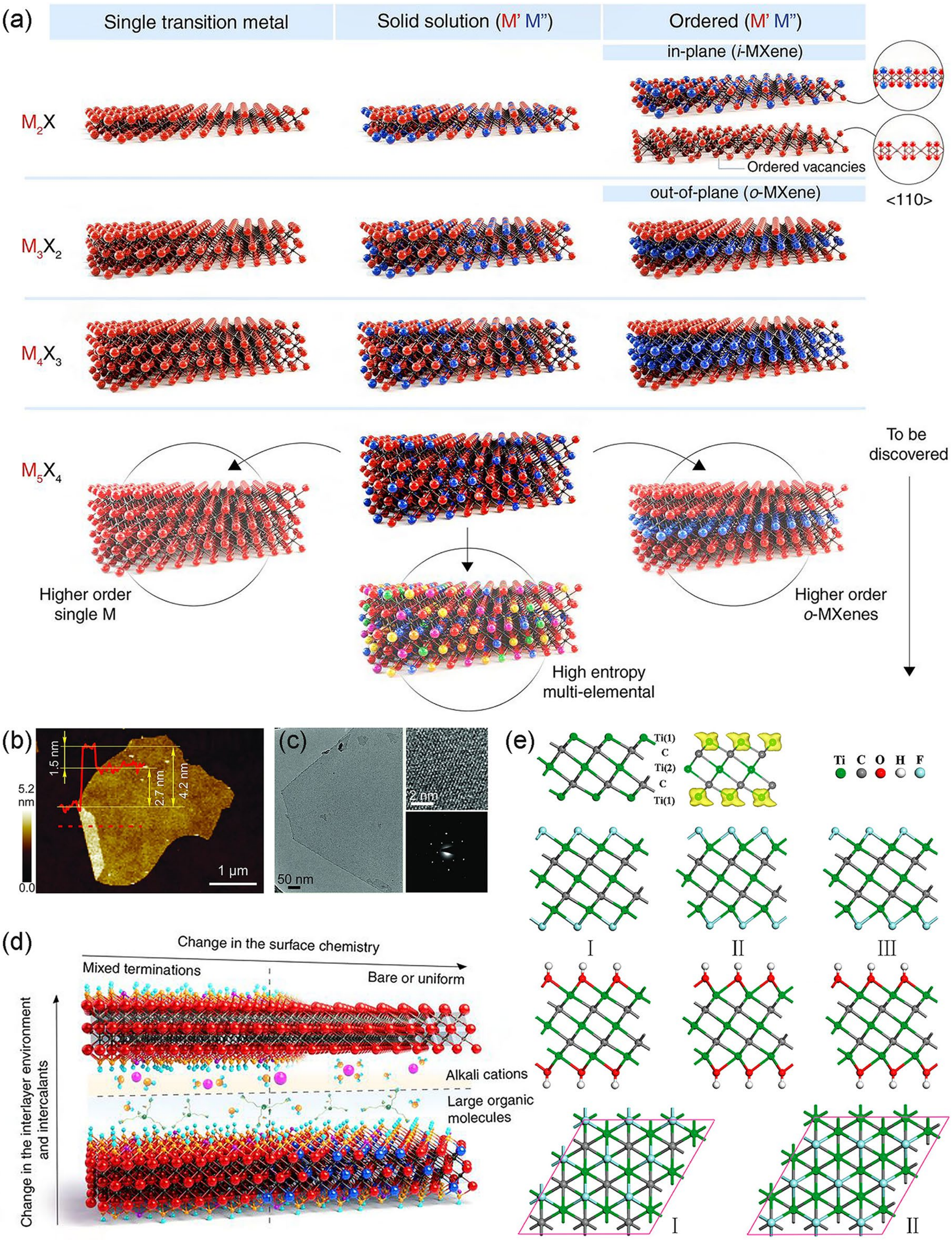

Fig. 4 **a** Schematic illustration of the MXenes with a general formula of $M_{n+1}X_nT_x$ [35]. Copyright 2021, The American Association for the Advancement of Science. **b** The AFM image of a folded $Ti_3C_2T_x$ flake on Si/SiO_2; **c** The HRTEM image and SAED image of $Ti_3C_2T_x$ [93]. Copyright 2016, Wiley–VCH. **d** Schematic illustration of the surface of MXenes is covered with various terminations [35]. Copyright 2021, The American Association for the Advancement of Science. **e** Schematic illustration of the optimized geometries of the free-standing Ti_3C_2 monolayer and its fluorinated and hydroxylated structural forms [102]. Copyright 2012, American Chemical Society

3 Photothermal Properties and Antibacterial Mechanisms of MXenes

Over the past decade, there have been plenty of studies concentrating on 2D materials for their bactericidal applications. The various antibacterial mechanisms of 2D materials, such as graphene (with physical insertion and chemical disruption) [104], MoS_2 (with enhanced conjugation of bacterial/PTT), WS_2 (with ROS release/damage the structural integrity of bacterial membrane), g-C_3N_4 (with photocatalytic self-cleaning), black phosphorus (with ROS release/membrane damage) have also been researched [105]. Intriguingly, rich tunability and promising new antibacterial strategies make MXenes stand out from numerous two-dimensional materials. Various advantages, including inherent 2D structure, satisfactory electromagnetic wave confinement and conversion capacity, and diverting LSPR effect, endow MXenes with satisfactory photo energy conversion ability, bringing in superb photo-induced antimicrobial effects [106]. The main target of photo-triggered antibacterial properties is to destroy bacterial cells in a particular way so as to perturb their life activity. Hence, the photothermal mechanisms of MXenes, mainly accounting for photo-induced antibacterial properties, are of tremendous importance and need to be described in detail. Interestingly, compared with sole PTT, various combined therapies with less light energy consumption show superior antibacterial potential and cost-effectiveness, achieving a desired synergistic effect [107, 108]. In this section, the photothermal properties of MXenes and their derivative antibacterial mechanisms will be systematically reviewed.

3.1 Photothermal Mechanisms of MXenes

The photothermal conversion capability of nanomaterials refers to their ability to absorb certain light energy and convert it into thermal energy. The photothermal conversion mechanisms on materials are primarily determined by their inherent molecular or crystal structure, inter-particle coupling, intra-particle coupling, and electron distribution [109]. Generally speaking, 2D MXenes enjoy exceptional advantages in photo-to-thermal conversion owing to their inherent large absorption surface, abundant free electrons distribution, and strong absorption in broadband solar spectrum, etc. [110]. Nevertheless, the investigation of photothermal behavior over MXenes was initiated only a few years ago, and we must continue to admit that a deep understanding of the photothermal mechanisms is still not established. A slew of pioneering research has been executed to our knowledge with the purpose of unravelling the mechanisms.

(i) MXenes and MXenes-based materials can efficiently absorb light energy in virtue of their satisfactory electromagnetic wave absorption capacity, which is an indispensable prerequisite for photothermal behavior. Shahzad et al. [86] pioneered the discovery of multiple internal reflection behaviors in $Ti_3C_2T_x$ flakes, which allowed them to dissipate and absorb the incident energy. On account of the high carrier concentration on the surface of MXenes, when electromagnetic waves reached the surface of the MXenes nanosheets, some waves would be reflected immediately. However, the induced local dipoles generated by the surface functional groups contributed to the absorption of incident light penetrating the $Ti_3C_2T_x$ structure. A considerable part of the electromagnetic waves entered the lattice structure and reflected multiple times between layers. When transmitted waves with less energy encountered the next MXenes flake, the same process occurred, resulting in an overall attenuation. As depicted in Fig. 6a, in this process of penetration, reflection, absorption, the energy of electromagnetic (EM) waves is gradually consumed and converted into heat [86].

(ii) The LSPR effect, through which surface carriers of metallic nanomaterials could be regulated to produce heat, also dominates the photothermal mechanisms of MXenes (Fig. 6b) [106, 111]. In general, metal nanoparticles exhibiting the LSPR effect are conducive to photothermal conversion [112, 113]. When light waves are incident on the interface between the metal and the dielectric components, the free electrons on the metal surface oscillate collectively [114]. The light waves couple with free electrons on the metal surface to form near-field electromagnetic waves propagating along the metal surface. If the oscillation frequencies of the electrons coincide with the frequencies of the incident light waves, resonance will occur, and the electromagnetic field will be confined to a small space on the metal surface and enhanced [115]. Intriguingly, Mauchamp et al. [116] demonstrated that $Ti_3C_2T_x$ exhibited plasmonic feature. The MXenes inherited from the MAX phase with metal-like characteristics possess a "semimetal" property [110]. Surface plasmons in MXenes are substantially dependent on the free charge carrier density on the surface, as reported for metals, semimetals, and semiconductors [117]. In this context, $M_{n+1}X_nT_x$ is known to exhibit an evident metal-like free electron density, which is closely related to the abundant surface-terminated moieties (T_x) [118]. Through spatially resolved ultra-high-resolution analysis, the longitudinal and transversal surface plasmson modes and the inherent interband transition sustained by flakes of MXenes could be unambiguously verified [117]. Profoundly, each monolayer in an MXenes flake behaves like an isolated sheet, sustaining a unique set of surface plasmon modes, revealing the particular 2D structure of MXenes and their fundamental divergence from "traditional" plasmonic metals [117]. Particularly in the visible and near-infrared ranges, MXenes exhibit longitudinal and transversal surface plasmon modes [35]. For example, two enhanced absorption peaks were observed in the absorbance spectra of $Ti_3C_2T_x$ composite at 610 and 1148 nm, which was caused by LSPR strongly enhancing the light-matter interaction (Fig. 6c) [111]. These two enhanced absorption bands in the visible and NIR regions allow the $Ti_3C_2T_x$ nanosheets to achieve a rapid sunlight-harvesting and photothermal conversion. Figure 6d displays the real-time dependence of temperature change, which also represented the switchable photothermal conversion performance [111]. Furthermore, it was reported that with the increase of the dispersion concentration of MXenes in the solvent, the corresponding absorption intensity and spectral irradiance were also increased [106]. Based on the advances in understanding the photo-to-thermal conversion mechanisms over MXenes, we have plotted the following figure to clearly illustrate this process (Fig. 5). Moreover, heat induced by PTT could boost the permeability of the bacterial cell membrane and speed up the cellular penetration of metal ions and ROS produced by PSs, thus achieving a desired synergistic treatment mode.

As a rule, the absorbed energy can be quantified by measuring the area under the solar spectral irradiance curve. MXenes possess plasmonic peaks covering the entire visible and near-infrared spectral region, and they also exhibit intense absorption in the ultraviolet range on account of interband transitions. As can be seen in Fig. 6e, the curve nearly overlapped with the spectral solar irradiance when the mass fraction of $Ti_3C_2T_x$ was 0.05 wt%, indicating a broadband absorption ability in 200–1500 nm wavelength [106]. Therefore, most of the radiant energy was absorbed and directly converted into heat. In practical measurements, the photothermal conversion of MXenes when exposed to various lights is confirmed. The highest reported internal photothermal conversion efficiency of $Ti_3C_2T_x$ could reach a shocking value of 100% [81]. Under the irradiation of 808 nm NIR light, the temperature of $Ti_3C_2T_x$ suspension with a low concentration of 10 μg mL^{-1} quickly reached 90 °C within 500–600 s at a power density of 5.43 W cm^{-2} (Fig. 6f) [119]. Meanwhile, the suspension also exhibited stable recurrent photothermal response to several light on–off cycles, even under NIR irradiation with high power density, which indicated their acceptable reusability and stability. The photothermal conversion efficiency of $Ti_3C_2T_x$ measured under 808 nm NIR light is superior to other reported photothermal materials, such as Cu_9S_5 (25.7%), Prussian Blue (41.4%), Au nanorods (21%), and nanovesicles (37%) (Fig. 6g) [119]. When 0.02 wt% $Ti_3C_2T_x$ nanosheets were exposed to simulated sunlight irradiation with the energy intensity of 0.1 W cm^{-2}, the maximum temperature rise was higher than other studied materials, including graphitic carbon (ZNG), ZrC, and reduced graphene oxide (rGO), as depicted in Fig. 6h [106]. The satisfactory photothermal conversion property ensures MXenes stand out from numerous 2D materials, promoting their potential in antibacterial applications where the temperature is one of the determining factors.

3.2 Photothermal and Photothermal-derived Antibacterial Mechanisms over MXenes

3.2.1 Photothermal Therapy over MXenes

The effect of heat on bacteria has been widely studied. In general, the cellular structures and substances affected by heat are the cytomembrane, nucleoid, peptidoglycan cell wall, ribonucleic acid (RNA), ribosomes, and diverse enzymes [120]. The lethality of heat is based on the destruction of at least one pivotal component beyond a critical threshold, which results in the inhibition of life activity of the bacteria [120]. PATs with high photo-to-thermal conversion efficiency heat up under light irradiation, which

https://doi.org/10.1007/s40820-022-00901-w

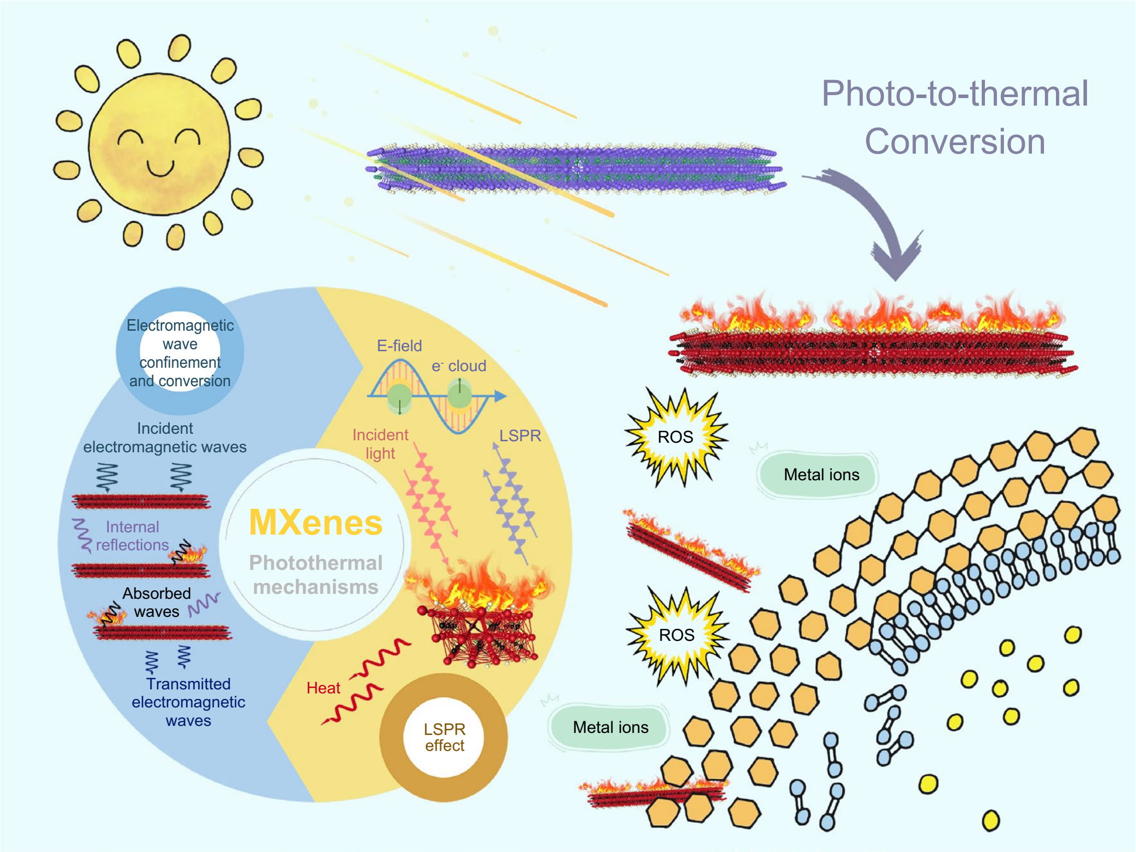

Fig. 5 The schematic photothermal mechanisms of MXenes account for superb photo-induced antimicrobial effects

seriously affects the life activities of surrounding pathogens. Moreover, MXenes can be unquestionably used as "nanothermal blades" owing to their excellent photothermal properties and inherently sharp 2D structures (Fig. 7a) [121]. Moreover, 2D flakes could be prepared into quantum dots, sequentially gaining various advantages, including high aqueous dispersibility, chemical stability, excellent optical property and easy functionalization [122–124]. Highly dispersed MXenes quantum dots exhibited whopping extinction coefficient and ultrahigh photothermal conversion efficiency, working as lethal "flocking nanothermal blades" to pathogenic cells [125].

Upon light irradiation, MXenes will effectively absorb and convert the light energy into heat, leading to the dramatic temperature rise on their surfaces, and this process will accelerate the death of the surrounding bacteria (Fig. 7b) [37]. The cell membrane, composed primarily of proteins, lipids, and polysaccharides, is significantly affected by heat generated on MXenes. Some studies have shown that membrane damage is linked to cell inactivation because of its partial loss of functionality, and the resulted imbalance of intracellular homeostasis has been demonstrated: disorganization in the entrance and outflow of several components [126, 127], suffocation of respiration activity [127] and loss of pH homeostasis [128]. The high temperature could also remarkably promote the permeability of pathogenic microorganisms' membranes, thus enhancing ROS or metal ions with antibacterial ability to infiltrate (this section will be discussed in detail next).

DNA is an essential molecule for bacterial survival, and its direct implication in the inactivation is undoubted. Upon exposure to heat, mutation frequency would increase in surviving populations, revealing that heat treatment gives rise to the irreversible damage of DNA [129]. Proteins exist in bacterial cells, either as structural proteins or as enzymes. Relevant research has demonstrated that hyperthermia would also cause protein denaturation and aggregation in bacterial cells when the temperature rises to an unbearable level

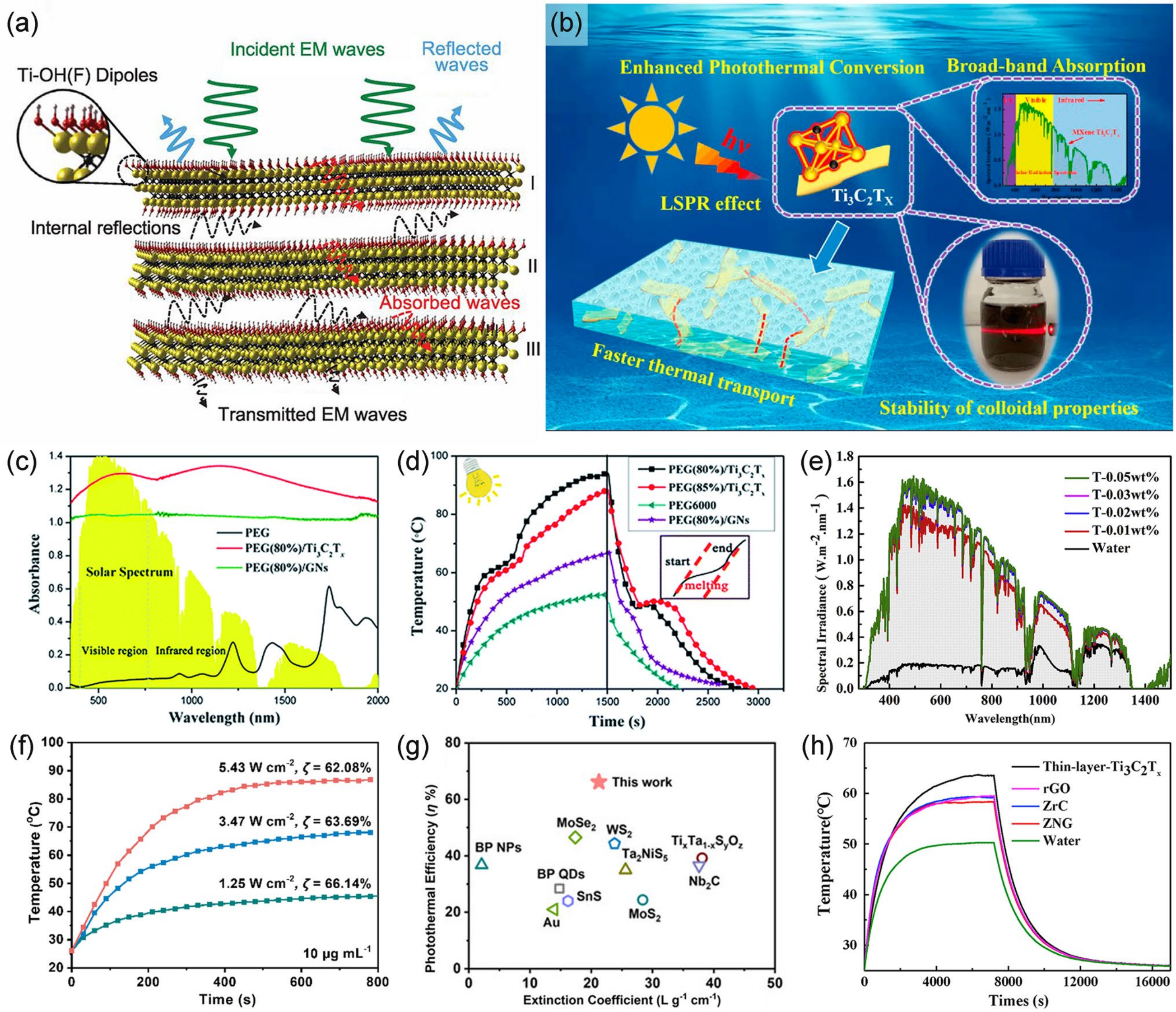

Fig. 6 **a** Schematic illustration of electromagnetic wave penetration/reflection/absorption [86]. Copyright 2016, The American Association for the Advancement of Science. **b** Schematic illustration of the radiation energy conversion mechanism of $Ti_3C_2T_x$ [106]. Copyright 2020, Elsevier. **c** Absorbance spectra of polyethylene glycol (PEG)/$Ti_3C_2T_x$ composite; **d** Temperature evolution curves of the PEG/$Ti_3C_2T_x$ composites under the simulated sunlight irradiation [111]. Copyright 2019, Royal Society of Chemistry. **e** The spectral irradiance of $Ti_3C_2T_x$ with different concentrations [106]. Copyright 2020, Elsevier. **f** Photothermal response of $Ti_3C_2T_x$ under 808 nm NIR light with various power; **g** Comparison between reported photothermal agents and $Ti_3C_2T_x$ in terms of mass extinction coefficient and photothermal conversion efficiency [119]. Copyright 2021, Wiley–VCH. **h** The temperature of nanofluids containing different nanoparticles with the same mass fraction (0.02 wt%) [106]. Copyright 2020, Elsevier

[130, 131]. Heat-induced protein denaturation could lead to functional loss in a variety of ways. Detoxifying enzymes, such as DNA repair enzymes, chaperones, proteases, and superoxide dismutase, which play a significant role in the self-regulation mechanism, are proven highly sensitive to heat [120]. Therefore, massive proteins will lose their function in bacterial cells if they are already thermally injured. Bacteria that have undergone photothermal treatment are almost impossible to develop antibiotic resistance by facilitating metabolism and reducing absorption [11].

Considering that MXenes exhibited high photothermal conversion capacity under light irradiation [23, 132, 133], the light-triggered antibacterial processes of MXenes could be inferred as follows: MXenes with sharp edges are

https://doi.org/10.1007/s40820-022-00901-w

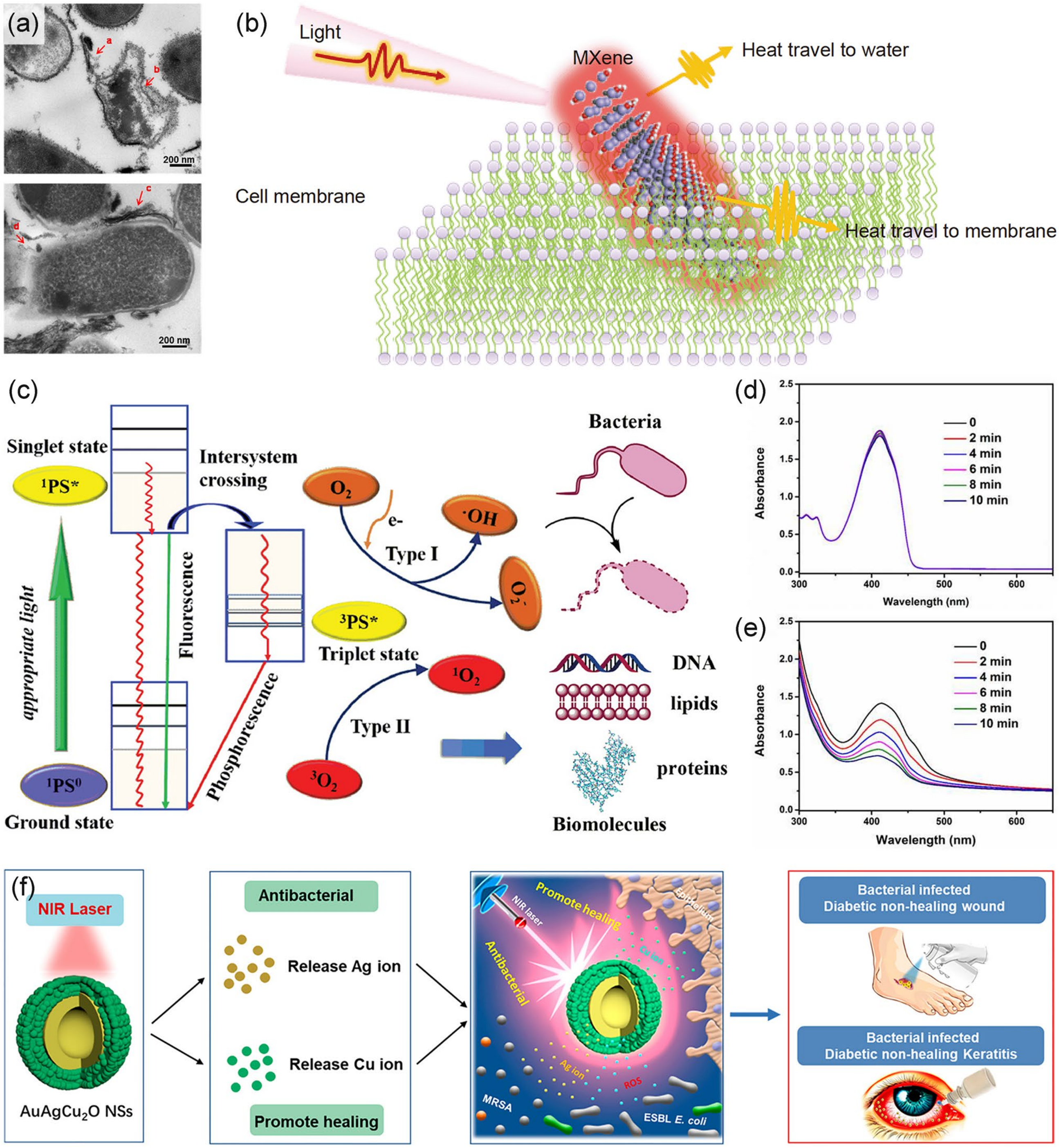

Fig. 7 **a** TEM images of diverse bacteria treated with 200 μg mL^{-1} of $Ti_3C_2T_x$ for 4 h [121]. Copyright 2016, American Chemical Society. **b** Schematic illustration of antibacterial mechanisms of MXenes with photothermal effect [37]. Copyright 2021, Springer Nature. **c** Photodynamic therapy mechanism of PSs under light irradiation [135]. Copyright 2019 Wiley–VCH. **d** Detection of DPBF's singlet oxygen generation upon 808 nm NIR light irradiation; **e** Detection of singlet oxygen generation over $Ti_3C_2T_x$ upon 808 nm NIR light irradiation [38]. Copyright 2017, American Chemical Society. **f** NIR-activated Ag ions and Cu ions kill bacteria and improve wound healing [108]. Copyright 2020, American Chemical Society

feasible to adhere to or insert into pathogenic cells, and at the same time, irradiation energy of light absorbed by MXenes nanosheets significantly increases the temperature of MXenes, as a result of which the generated hyperthermia facilitates the ablation of bacterial structures, resulting in pathogenic bacteria death. Undoubtedly, PTT has become a well-trusted antibacterial therapy due to antibiotics-independent performance and selective hyperthermal treatment.

3.2.2 Photothermal/Photodynamic Synergistic Therapy and Other Photothermal- derived Therapy

Nevertheless, sole PTT cannot always meet the demand for antimicrobial applications. For example, higher temperatures exceeding the tolerance limits of healthy cells might be required if PTT is exclusively used to eradicate biofilms or drug-resistant bacteria, which greatly limits its potential in vivo applications [2]. Synergistic therapies, such as PTT/PDT and PTT/metal ions incursion, have emerged and received extensive attention in recent years as new strategies to solve these problems. For the combined approaches between PTT and PDT, the generated heat through photothermal conversion could increase the permeability of cell membranes and thus enhance the penetration ability of ROS into cells [2]. Photo-induced ROS, such as singlet oxygen ($^1O_2$), super oxide anions (O_2^-), and hydroxyl radical, has been widely acknowledged as powerful weapons to cause oxidative stress and sequentially sabotage the integrity of cytomembranes [26, 134]. Photodynamic therapy employs photo-responsive substances to generate ROS, which could further oxidize the surrounding biomolecules such as nucleic acids, lipids, and proteins to cause devastating damage to the target cells (Fig. 7c) [135]. Based on the ROS formation pathways, PDT is categorized into two types, namely, type I and type II [2, 135]. The PSs used in PDT are basically in the ground state ($^1PS^0$) and become excited to a singlet state ($^1PS^*$) after being irradiated with a specific light source. Through intersystem crossing, the electron transitions from the short-lived singlet state to the long-lived triplet state ($^3PS^*$). In type I process, $^3PS^*$ transfers one electron directly to the adjacent substrate, generating free radicals or radical ions, mainly including O_2^- and •OH. O_2^- is an essential intermediate in the biosystem for generating H_2O_2 employing dismutation in the presence of superoxide dismutase or by one-electron reduction. Ulteriorly, the highly cytotoxic •OH can be obtained under the one-electron reduction of H_2O_2. Type I reaction occurs primarily on bacterial cell membranes, with unsaturated phospholipid molecules to extract hydrogen. These molecules further react with oxygen and form lipid peroxides, thereby disrupting structural integrity and making bacterial cell membranes more permeable. In the Type II process, the energy of the 3PS* is rapidly transferred to molecular oxygen ($^3O_2$) due to the electron spin multiplicity, leading to the excitation of $^3O_2$ from the ground state to the excited singlet state, producing the so-called singlet oxygen ($^1O_2$) [136]. $^1O_2$ is the most destructive ROS and can directly oxidize critical biomolecules in cells, such as lipids, peptides, and enzymes [137, 138]. The ROS generation ability of MXenes under irradiation could be evaluated by probes. For example, when the suspension of $Ti_3C_2T_x$ nanosheets was irradiated with 808 nm NIR light, the absorbance of 1, 3-diphenylisobenzofuran (DPBF) as probe molecules was much lower than that of the control group without nanosheets, and the absorption intensity decreased with irradiation time increasing (Fig. 7d, e) [38]. The decrease in absorbance indicated that $^1O_2$ was trapped by DPBF, verifying that $^1O_2$ was generated from $Ti_3C_2T_x$ nanosheets under NIR irradiation. Furthermore, the generation of ROS could be enhanced when MXenes were combined with other components, such as metal sulfides and metal oxide semiconductors, to form the nanocomposites [139, 140].

Bactericidal metal ions exhibited remarkable bactericidal effects by inactivating intracellular proteins and destroying bacterial membranes (Fig. 7f) [108]. These metal ions could noninvasively release and maintain their excellent bactericidal ability at low doses without exhibiting side effects when combined with PTT and PDT. For instance, Cu species could be anchored on the surface of MXenes in the form of sulfide or oxide, greatly improving the separation of the photo-generated electron–hole pairs upon irradiation, and as a result of this, enhanced ROS generation and accelerated penetration of copper ions can be expected [25, 139]. In general, by making full use of the physical puncture contribution of MXenes, the hyperthermia of PTT, and the facilitated penetration of ROS or metal ions, MXenes-based materials could bring in rapid destruction of the cell membranes as well as the accelerated collapse of the cellular homeostasis.

4 Applications of MXenes in Antibacterial and Related Fields

As discussed in the previous section, MXenes-based materials have been regarded as a well-reliable antibacterial candidate for their remarkable photo-to-thermal conversion capacity as well as other photothermal-derived synergistic therapies potential. Multifunctional photo-responsive MXenes-based materials that integrate the advantages of photothermal effect and antibacterial activity are increasingly used in many fields. In this section, we summarize the state-of-the-art achievements utilizing MXenes-based materials for in vitro/vivo clinic trials, water purification and smart fabrics where bacteria-killing is necessary.

4.1 In Vitro Antibacterial Applications

In the last decade, the application prospect of MXenes in antibacterial has been exhaustively confirmed and rapidly developed. However, pure MXenes cannot always meet the demand for photothermal sterilization. Hence, synergistic therapies such as MXenes/other antimicrobial agents and MXenes-based photodynamic hybrids have been regarded as new countermeasures.

4.1.1 Pure MXenes

Owing to their extremely high photothermal conversion ability, outstanding biocompatibility, fascinating antibacterial properties and low cytotoxicity, MXenes have attracted extraordinary attention for biomedical applications [141]. For instance, as one of the earliest and most widely used MXenes, $Ti_3C_2T_x$ exhibited the feature of high efficacy, small dosage, and fast function in antibacterial applications. According to Rosenkranz et al. [78], the use of few-layered $Ti_3C_2T_x$ (FX) and multilayered $Ti_3C_2T_x$ (MX) nanosheets as antibacterial PTT against *E. coli* and *S. aureus* was feasible. The biocompatibility experiment showed that certain eukaryotic cell lines were less cytotoxic when exposed to few-layered $Ti_3C_2T_x$ nanosheets. And for the bacteria treated with few-layered $Ti_3C_2T_x$, the damage of cell membrane and the loss of contents were more serious than the multilayered $Ti_3C_2T_x$ group (Fig. 8a) [78]. With the effect of PTT, $Ti_3C_2T_x$ destroyed the protective membrane and further inactivated the inherent bioactive matrix promptly. Upon 808 nm NIR light irradiation, significant antibacterial effects could be observed in a suspension of $Ti_3C_2T_x$ nanosheets after only 20 min (Fig. 8b) [37]. $Ti_3C_2T_x$ nanosheets have been found to show an obvious killing effect on a variety of bacteria, including methicillin-resistant *Staphylococcus aureus* and vancomycin-resistant *Enterococci* [37]. Furthermore, the rapid antibacterial strategy could suppress methicillin-resistant biofilms by destroying their structures as well as erasing the bacteria within them (Fig. 8c). The survival rate of bacteria in the biofilm of the experimental group was reduced by 95% compared to the control (Fig. 8d, e). Similar to $Ti_3C_2T_x$, V_2C displayed high structural stability and strong NIR absorption properties and has also been reported for photothermal ablation of bacteria. Zada and colleagues developed an algae extract-based controllable and green delamination approach to exfoliate V_2C nanosheets with antimicrobial activity (Fig. 8f) [142]. The thermal images showed that the temperature of 80 μg mL^{-1} V_2C nanosheets could reach above 50 ℃ within 5 min under the irradiation of 808 nm NIR light, which exceeded the tolerance level of *E. coli* and *B. subtilis* (Fig. 8g). In the laser on/off cycles (five times off and on), the temperature changes of V_2C nanosheets suspension showed a negligible fluctuation and an insignificant decline, indicating satisfying photothermal stability of V_2C nanosheets. Consequently, this suspension achieved an antibacterial efficiency of over 99.5% using V_2C nanosheets with reliable photothermal properties.

4.1.2 Composites of MXenes and Other Antimicrobial Agents

The combination of MXenes with other antimicrobial agents offers a promising way to enhance the ability to inhibit bacteria reproduction. Nanoscale silver is an encouraging antimicrobial agent because of its broad spectrum and long-lasting antibacterial activity. It has been proven a promising strategy by decorating silver nanoparticles on the surface of 2D MXenes to achieve desired sterilization performance. Zhu et al. [41] reported the representative case study on utilizing Ag/$Ti_3C_2T_x$ for synergistic antibacterial effect (Fig. 9a). In this work, silver ions were firstly adsorbed and then reduced by sodium citrate on negatively charged $Ti_3C_2T_x$ nanosheets producing the Ag/$Ti_3C_2T_x$ composites. Ag/$Ti_3C_2T_x$ suspension of 200 μg mL^{-1} showed inferior antibacterial activity in the dark, but the composites could

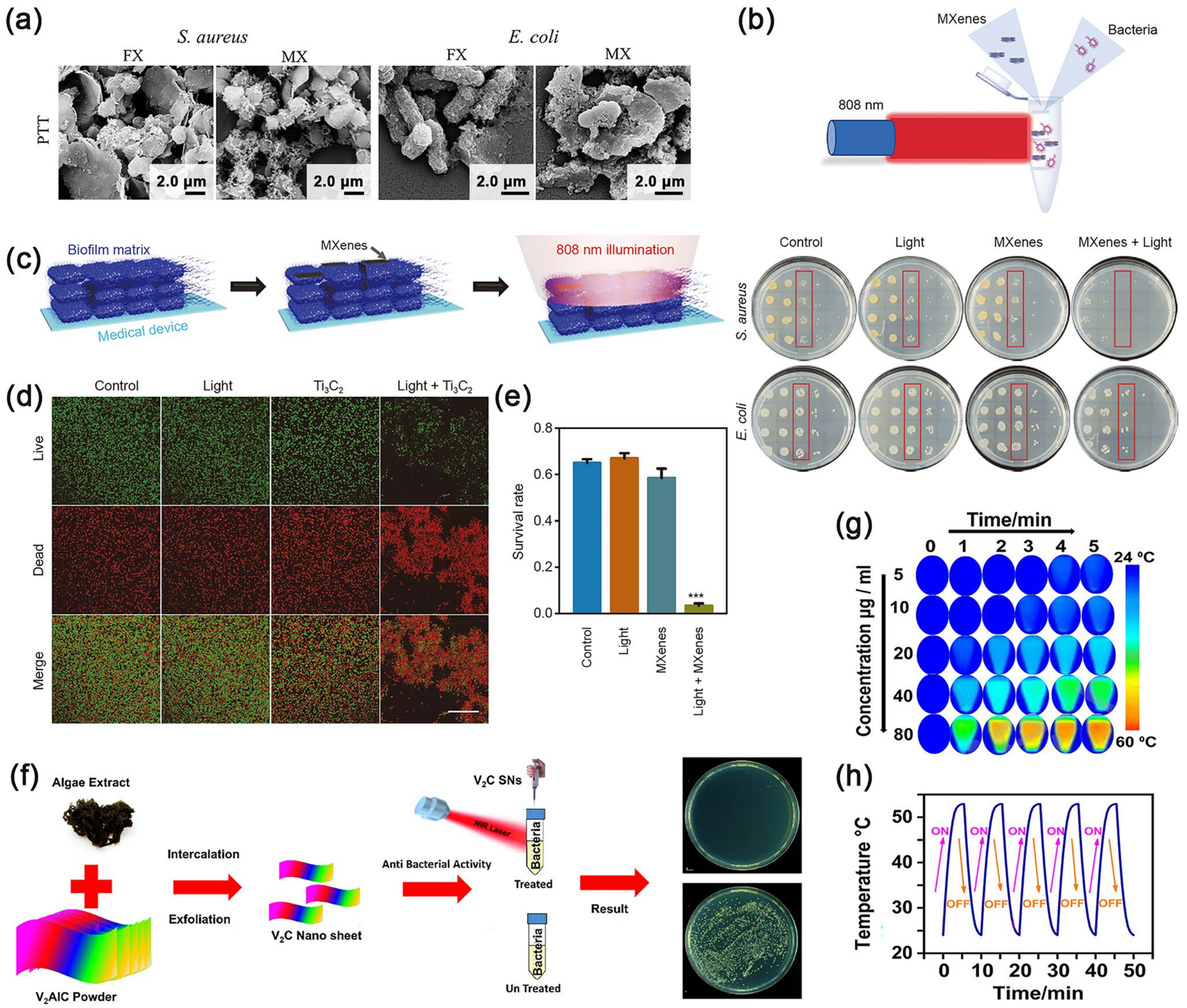

Fig. 8 **a** SEM images of *S. aureus* and *E. coli* after treatments with few-layered $Ti_3C_2T_x$ (FX) and multilayered $Ti_3C_2T_x$ (MX) along with PTT [78]. Copyright 2021, Elsevier. **b** Colony-forming units images of *S. aureus* and *E. coli* without and with 20 min light treatments; **c** Schematic illustration of bacterial biofilms treated with MXenes and NIR light; **d** Fluorescence images of bacterial biofilms treated with MXenes and NIR light; **e** Survival statistics of bacterial biofilms treated with MXenes and NIR light [37]. Copyright 2021, Springer Nature. **f** Synthesis of V_2C and its synergistic photothermal antibacterial effect; **g** Thermic photograph of V_2C under NIR light; **h** Heating and cooling cycles of 40 μg mL^{-1} V_2C under NIR light [142]. Copyright 2021, American Chemical Society

effectively kill all bacteria when exposed to 808 nm NIR light irradiation (Fig. 9b). The SEM results were also in line with the antibacterial tests, where the $Ag/Ti_3C_2T_x$ under NIR irradiation showed palpable synergistic antibacterial performance. In the high-resolution image, it was evident that bacteria exposed to light underwent cytoplasm leakage and cytolysis (Fig. 9c). The antimicrobial efficacy of silver nanoparticles is associated primarily with Ag^+ ions release. In the work of Nie et al. [143], they soaked the thin film containing $Ti_3C_2T_x$/Ag in a certain volume of solution and irradiated it with a Xe lamp (500 W, 31.45 W cm^{-2}). According to Fig. 9d, e, under light illumination, the concentration of released silver ions was 0.46 mg mL^{-1}, almost 300 times relative to the control group. It indicated that light promoted the release of Ag ions, and this process resulted in enhanced antimicrobial efficiency.

CuS is also a widely recognized antibacterial agent with excellent light absorption properties and Cu^{2+} release ability.

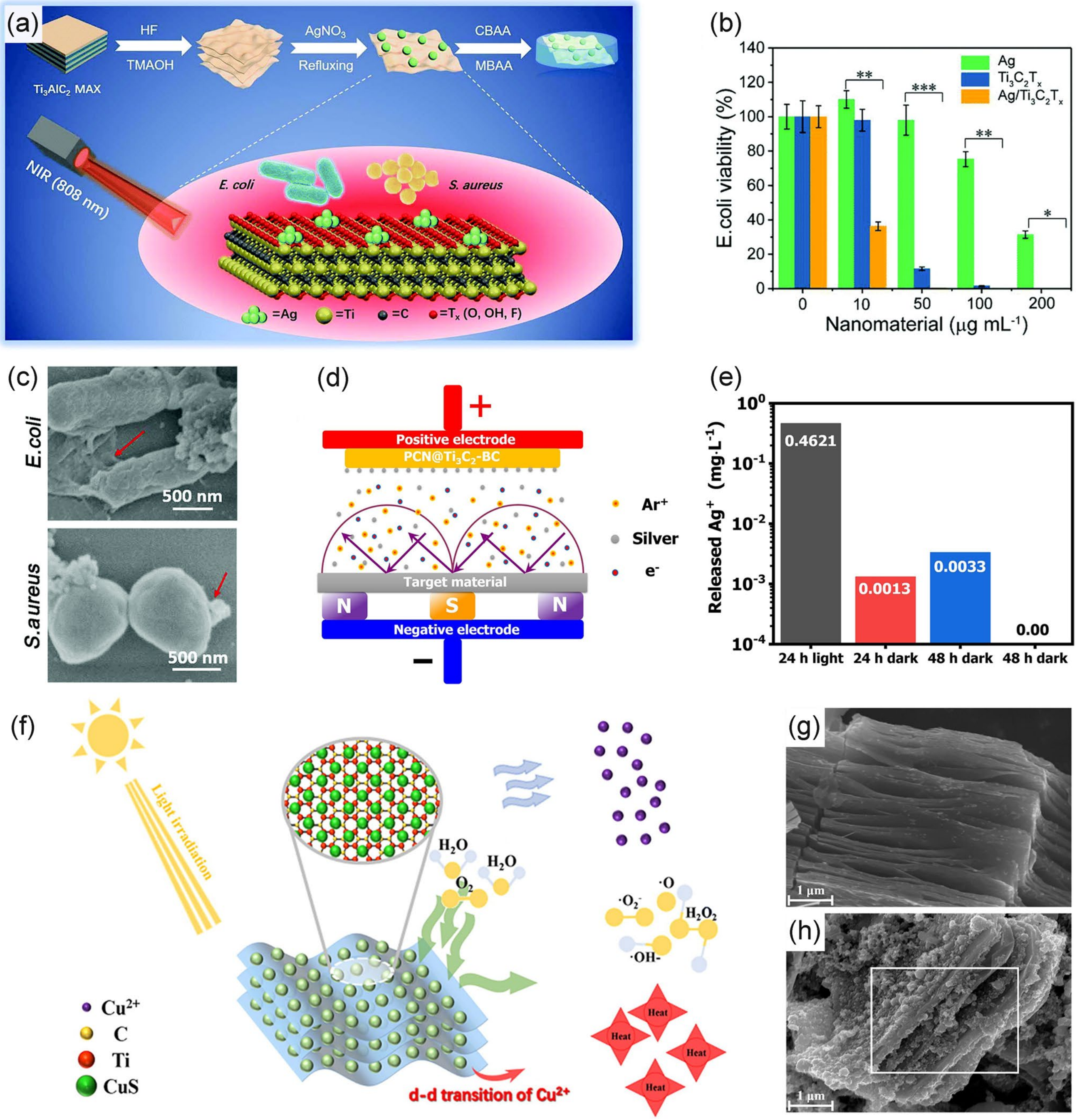

Fig. 9 **a** Schematic illustration of photothermal antibacterial properties of Ag/$Ti_3C_2T_x$; **b** Relative bacteria viability with NIR light irradiation after incubation with different concentrations; **c** HRTEM images of *E. coli* and *S. aureus* were treated with Ag/$Ti_3C_2T_x$ under NIR light [41]. Copyright 2020, Royal Society of Chemistry. **d** Schematic illustration of the film loaded with Ag$^+$; **e** Schematic illustration of the release of Ag$^+$ under different treatments [143]. Copyright 2021, Elsevier. **f** Schematic illustration of antibacterial mechanism of $Ti_3C_2T_x$/CuS; **g** SEM image of multilayered $Ti_3C_2T_x$; **h** SEM image of $Ti_3C_2T_x$/CuS [139]. Copyright 2021, Elsevier

However, the incorporation of CuS into MXenes by simple physical mixing makes it difficult to achieve a controlled release of Cu^{2+}, and excessive local accumulation may cause negative effects, ultimately leading to poor antibacterial activity. Recent studies indicated that MXenes are ideal support materials for fabricating nanohybrids and the surface decoration of CuS nanoparticles on them through in situ growth has emerged as an efficient method. In a recent study, Li et al. [139] prepared NIR responsive MXenes/CuS composites through the reaction between C_2H_5NS and Cu^{2+} adsorbed on the surface of multilayered $Ti_3C_2T_x$, achieving the controllable release of Cu^{2+} could be achieved (Fig. 9f). As shown in the SEM images, CuS nanoparticles with diameters ranging from 100 to 500 nm were uniformly grown on the multilayered $Ti_3C_2T_x$ surface (Fig. 9g, h). Under the irradiation of NIR light, the release of Cu^{2+} was significantly enhanced. Owing to the synergistic contributions from the photothermal effects of MXenes and CuS and the enhanced release of bactericidal Cu^{2+} ions, the antibacterial efficiency of the MXenes/CuS group exceeded 99% against both *E. coli* and *S. aureus*. Such results underscored the importance of the simultaneous action of hyperthermia and antibacterial metal ions, revealing the great potential of synergistic therapy.

4.1.3 *MXenes-Based Photodynamic Hybrids*

As photodynamic antibacterial strategies receive considerable research interest, MXenes-based hybrid systems are extensively investigated for their potential in ROS generation [16, 144]. However, the narrow bandgap of the $Ti_3C_2T_x$ nanosheets (about 1.69 eV) severely hampers their performances due to the fast recombination of photo-generated electron-holes, which results in the limited release of ROS [51]. Previous research indicated that some photosensitive nanomaterials such as metal nanoparticles, metal oxides, carbon-based nanomaterials, and metal chalcogenides had shown their prospects in bacteria-killing under light irradiation [10]. However, the photo-induced ROS production on these materials is heavily impaired once without the cocatalysts, which usually act as electron traps and reactive sites. Accordingly, the establishment of heterojunctions between these photosensitive materials with metallic MXenes is considered an effective modified strategy for significantly separating photo-generated electron–hole pairs and thus promoting ROS production [47]. Many groups have verified such strategy to achieve the desired antibacterial performance based on photo-induced approaches. As depicted in Fig. 10a a 2D/1D heterojunction between $Ti_3C_2T_x$ and cobalt nanowires has been presented, and the composites exhibited NIR-triggered photothermal and photodynamic synergistic antibacterial activity [39]. The electrons were excited from the valence band (VB) to the conduction band (CB) of $Ti_3C_2T_x$ with NIR laser irradiation and transferred quickly to the surface of cobalt nanowires. In this way, electrons gathered on the surface of the cobalt nanowires and holes accumulated on the VB of $Ti_3C_2T_x$, which hindered the recombination of electrons and holes. The adsorbed oxygen captured photogenerated electrons to generate ROS, leading to the diffusion of ROS from the heterojunction to the whole system. In comparison with the control group, the MXenes/Co group caused obvious bacterial lysis, as confirmed by SEM and confocal images (Fig. 10b, c). Analogously, Li et al. [16] designed $Ti_3C_2T_x/Bi_2S_3$ composites and found that the Schottky barrier at the interfaces forcefully enhanced the amount of generated ROS (Fig. 10d, e). As a result, the composites could feasibly kill 99.92% of *E. coli* and 99.86% of *S. aureus* under 808 nm NIR irradiation within 10 min (Fig. 10f). It can be seen that the construction of heterojunctions provides new strategies for designing light-triggered devices for antibacterial applications. Here, the possibility that MXenes can be combined with a variety of nanomaterials opened up endless possibilities for such designs. To sum up, through the ingenious preparation of MXenes-based nanomaterials and subsequent appropriate modification, various photothermal-derived platforms could exhibit satisfactory in vitro bactericidal properties. We thoroughly investigated the literature database and summarized the advances in this topic by sorting their main components, antibacterial mechanisms, effects, and conditions, as shown in Table 3.

4.2 In Vivo Antibacterial Applications

Skin, serving as the largest organ and the first line of body defense, maintains stability in the interior environment when faced with external threats [147]. Nonetheless, infected dermis wounds may cause pain, amputations or even death and have emerged as one of the severest threats to global health security [27]. Sponge, bandages, and gauze are the most routinely used wound dressings, and they possess ordinary functions by forming a physical parclose or assimilating exudate. However, they are unable to perform the biochemical action of eliminating bacteria and promoting healing. Consequently, designing newfangled light-triggered wound dressings that can promote bacteriostasis, enhance granulation

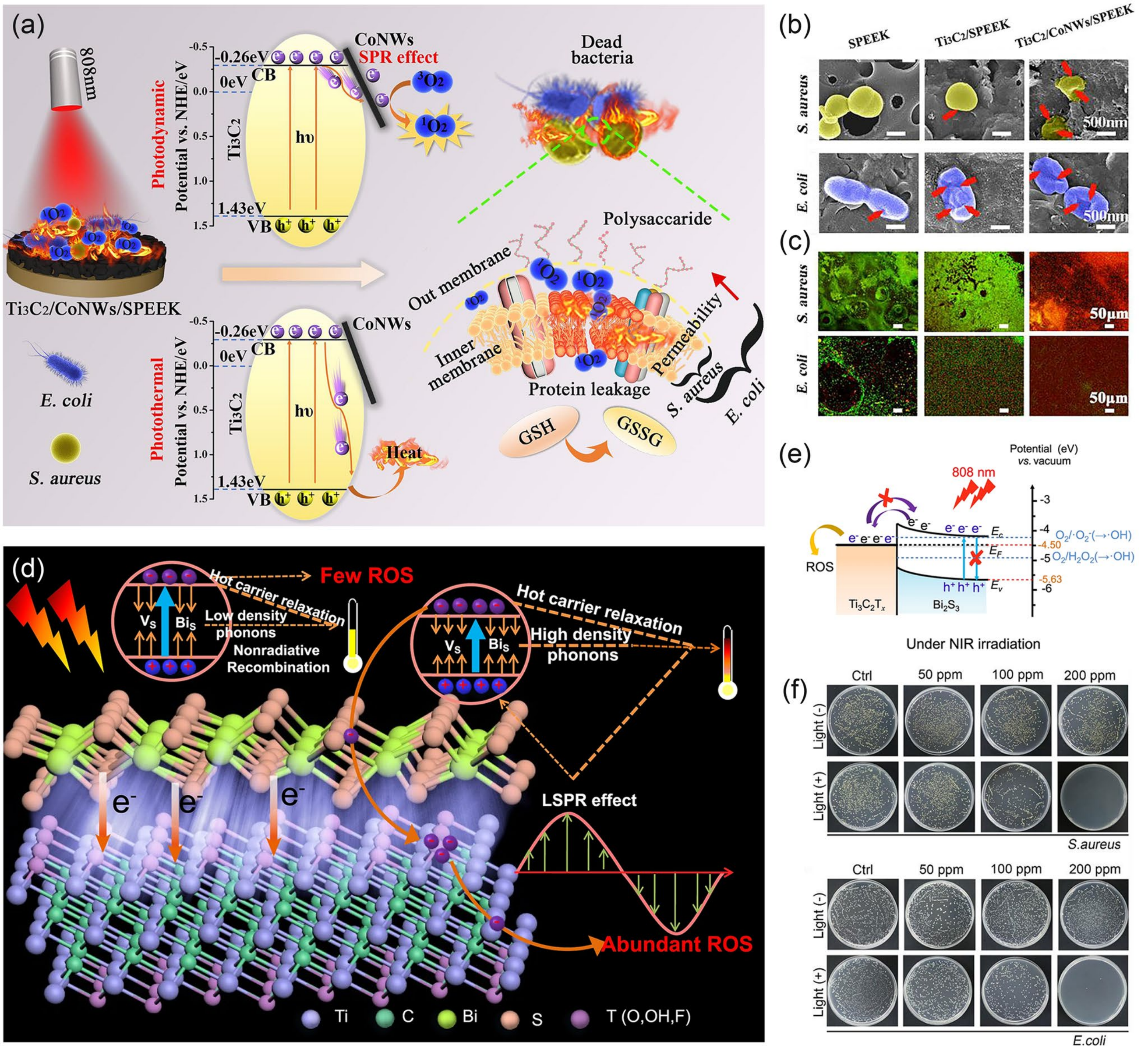

Fig. 10 **a** Schematic illustration of photothermal/photodynamic antibacterial property of MXenes/Co; **b** TEM images of *S. aureus* and *E. coli* were treated with NIR light; **c** Confocal images of *S. aureus* and *E. coli* were treated with NIR light [39]. Copyright 2020, Elsevier. **d** Schematic illustration of photodynamic and photothermal mechanism between $Ti_3C_2T_x$ and Bi_2S_3; **e** The mechanism of the enhanced yield of ROS via NIR-induced progress is based on the Schottky heterostructure; **f** Colony-forming units images of *S. aureus* and *E. coli* without and with 10 min NIR light treatments [16]. Copyright 2021, Springer Nature

tissue formation and accelerate cutaneous regeneration is desirable. To remedy bacteria-invaded stalled full-thickness wounds (Fig. 11a), Zhou et al. [22] group devised a nanoscale catalytic membrane (P-MX/AS@LOx) consisting of electrospun poly (lactic-co-glycolic acid) (PLGA) scaffolds, MXenes/Ag_2S (MX/AS) bio-heterojunctions, and lactate oxidase (LOx). The MXenes/Ag_2S bio-heterojunctions in the membrane not only exerted a mild photothermal effect and generated ROS under NIR light but also overwhelmed the hydroxyl radicals through Fenton-like reactions, which resulted in highly efficient synergistic sterilization. Upon exposure to NIR light, the temperature of the experimental group increased from 22.5 to 61.2 °C within 10 min, confirming the extraordinary efficiency of in vivo photothermal conversion (Fig. 11b). As shown in Fig. 11c, d, the nanoscale catalytic membrane remodeled stagnant chronic wounds into

Table 3 Summary of in vitro photothermal-derived antibacterial applications using MXenes-based materials

Main components	Antibacterial mechanisms	Light source	Concentration (μg mL^{-1})	Treatment time (min)	Bacteria	Effect	References
Few-layered $Ti_3C_2T_x$	PTT	808 nm, 5.7 W cm^{-2}	100	5	*E. coli*	> 85%	[78]
					S. aureus	> 95%	
$Ti_3C_2T_x$	PTT	808 nm, 0.4 W cm^{-2}	100	20	*E. coli*	> 85%	[37]
					S. aureus	100%	
$Ti_3C_2T_x$/Ag	PTT/Ag^+ release	808 nm, 1.5 W cm^{-2}	100	15	*E. coli*	100%	[41]
$Ti_3C_2T_x$/Ag	ROS generation/Ag^+ release	808 nm, 0.4 W cm^{-2}	1.56	30	*E. coli*	100%	[145]
			3.12		*S. aureus*	100%	
$Ti_3C_2T_x$/Ag	PTT/ROS generation/Ag^+ release	Xe lamp, 31.45 W cm^{-2}, 15 cm	–	30	*E. coli*	100%	[143]
					S. aureus	100%	
$Ti_3C_2T_x$/Ag/Cu_2O	ROS generation/Ag^+ release	T5 energy saving lamp	2000	720	*P. aeruginosa*	99.7%	[48]
					S. aureus	99.7%	
$Ti_3C_2T_x$/Au	PTT/ROS generation	808 nm, 2.0 W cm^{-2}	160	8	*E. coli*	99.3%	[28]
					B. subtilis	100%	
$Ti_3C_2T_x$/Co	PTT/ROS generation	808 nm, 1.5 W cm^{-2}	–	20	*E. coli*	92.7%	[39]
					S. aureus	80.1%	
$Ti_3C_2T_x$/Bi_2S_3	PTT/ROS generation	808 nm, 0.7 W cm^{-2}	200	10	*E. coli*	99.9%	[16]
					S. aureus	99.9%	
$Ti_3C_2T_x$/CuS	PTT/ROS generation/Cu^{2+} release	808 nm, 1.5 W cm^{-2}	500	720	*E. coli*	99.6%	[139]
					S. aureus	99.1%	
$Ti_3C_2T_x$/AgS	PTT/ROS generation	808 nm, 0.67 W cm^{-2}	500	20	*S. aureus*	99.9%	[17]
$Ti_3C_2T_x$/Cu_2O	ROS generation/Cu^{2+} release	–	40	1200	*S. aureus*	95.6%	[144]
					P. aeruginosa	97.0%	
$Ti_3C_2T_x$/TiO_2	ROS generation	White light	100	180	*E. coli*	97.4%	[140]
$TiVCT_x$	Physical damage/PTT	808 nm, 0.1 W cm^{-2}	40	30	*E. coli*	100%	[146]
					B. subtilis	100%	
V_2C	Physical damage/PTT	808 nm, 0.1 W cm^{-2}	40	5	*E. coli*	99.5%	[142]
					B. subtilis	99.5%	

regenerative wounds by killing bacteria, stopping bleeding, promoting angiogenesis, boosting collagen deposition and enhancing epithelialization.

Aside from membrane, hydrogels are also recognized as a new type of wound dressing because of their high water absorbing abilities and porous structure, showing promising potentials in promoting wound healing. Inspired by the hierarchical assembly of anisotropic structures across multiple length scales of muscles, Li et al. [148] designed an anisotropic MXenes@ polyvinyl alcohol (MXenes@PVA) hydrogel using a directional freezing-assisted salting-out method (Fig. 11e). Except for the excellent mechanical properties (stress up to 0.5 MPa, strain up to 800%), the hydrogel could also be used for local hyperthermia treatments at infected sites under 808 nm NIR irradiation. They employed a full-thickness *S. aureus*-infected wound model to evaluate the efficiency of MXenes@PVA hydrogel to cure infected skin wounds. As shown in Fig. 11f, g, the wound healing rate of the MXenes@PVA plus NIR group reached 98% after ten-day treatments, and most of the wounds were covered by new skin. The antibacterial activity of the experimental group was significantly higher than those of the control group, indicating that under NIR irradiation, MXenes@PVA hydrogel was effective in combating bacterial infection caused by *S. aureus* (Fig. 11h, i). MXenes@PVA hydrogel exhibited

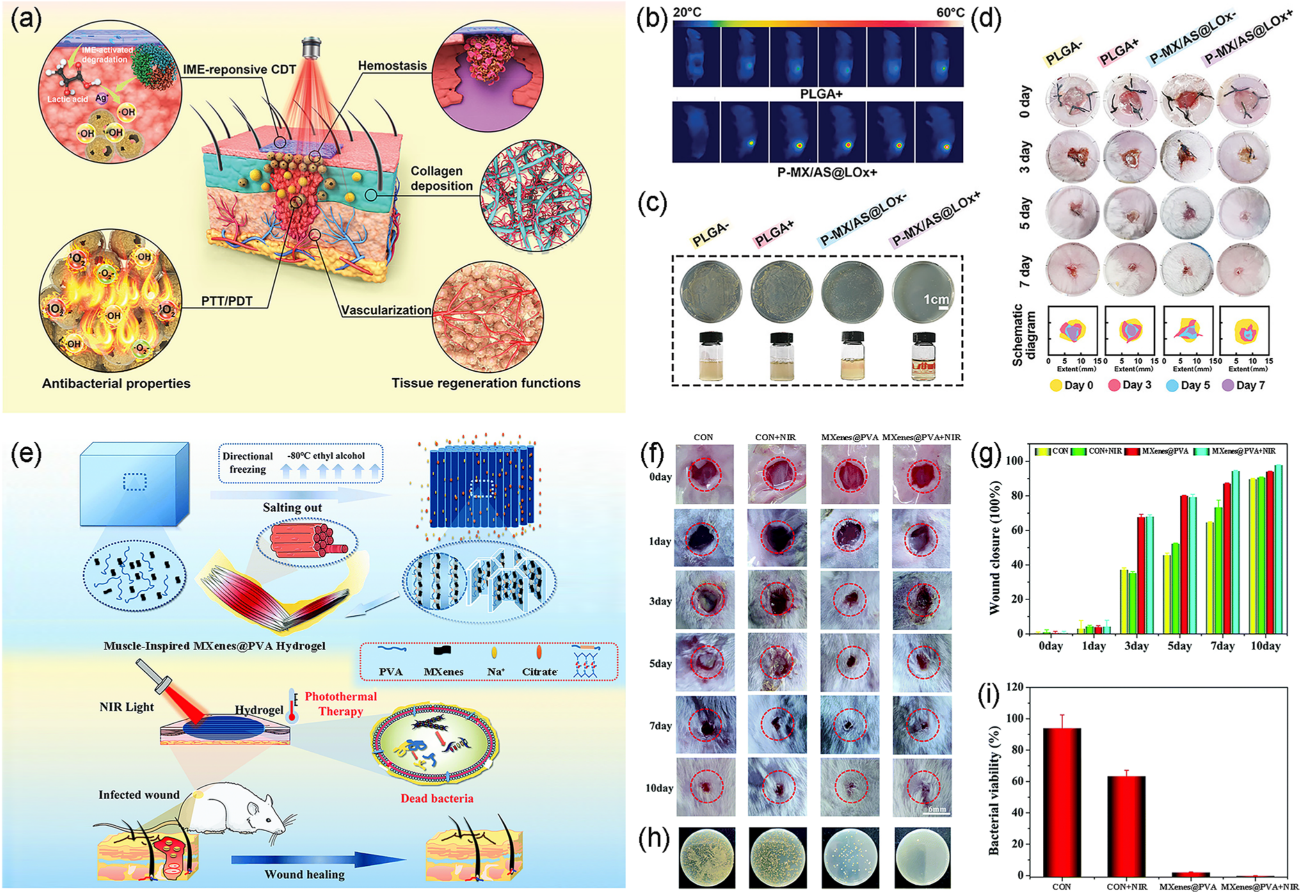

Fig. 11 **a** Schematic illustration of the antimicrobial and infected wound repair effects by nanocatalytic membrane; **b** Surface NIR images of membranes under NIR light irradiation for 10 min; **c** Colony-forming units images of the bacterial colonies after different treatments; **d** Photographs of *S. aureus*-infected wounds healing after treatments [22]. Copyright 2021, Wiley–VCH. **e** Schematic illustration of the antimicrobial and infected wound repair effects by MXenes@PVA hydrogel; **f** Photographs of healing of *S. aureus*-infected wounds in different treatment groups; **g** Wound contraction evaluations of healing of *S. aureus*-infected wounds in different treatment groups; **h** Colony-forming units images of the bacterial colonies different treatments; **i** Quantitative bacterial viability based on **h** [148]. Copyright 2022, Royal Society of Chemistry

high toughness, anisotropy, and antimicrobial properties, hinting it could be an attractive dressing for antibacterial wound healing. In addition to the above composites, $Ti_3C_2T_x/Ag_3PO_4$ [27], $Ti_3C_2T_x/MoS_2$ [149], $Ti_3C_2T_x/Bi_2S_3$ [16], $Ti_3C_2T_x/Ag$ [41], and Nb_2C [150] have all shown promising prospects for in vivo wound healing; the research progress could be found in Table 4.

4.3 Antibacterial Water Evaporation and Purification

In recent years, solar-driven interfacial water evaporation has received increasing attention as a practical water purification solution for water-scarce regions [152, 153]. In comparison with traditional desalination technologies, solar evaporation systems demonstrate high-efficiency, low-cost, and eco-friendly performances [154]. MXenes with 2D nanosheet morphology and strong photo absorption capacity from UV to infrared (IR) range are excellent candidates for the fabrication of solar evaporators [152]. When these nanoscale photo-heaters are incorporated into film or hydrogel systems, they offer versatile potential to design antibacterial soft materials. Ideally, photothermal materials with antibacterial activity are more demanding for water purification applications as no extra antibiotics are necessary. Antibacterial properties of solar evaporators could mightily extend their service life by suppressing the formation of biofouling and inactivating pathogens in the water to ensure the production of fresh, clean and

Table 4 Summary of in vivo photothermal-derived antibacterial applications using MXenes-based materials

Main components	Dressing strategy	Antibacterial mechanisms	Bacteria	Light source (808 nm)	Treatment time (min)	Wound temp. (°C)	References
$Ti_3C_2T_x/Ag_3PO_4$	Fibrous membrane	PTT/ROS generation/Ag^+ release	*S. aureus*	1.5 W cm^{-2}	10	58	[27]
$Ti_3C_2T_x/Ag_2S$/Lactate oxidase	Nanocatalytic membrane	Chemodynamic therapy/PTT/ROS generation/Ag^+ release	*S. aureus*	1.5 W cm^{-2}	10	61.2	[22]
$Ti_3C_2T_x/MoS_2$	2D bio-heterojunction	PTT/ROS generation/Mo^{4+} release	*S. aureus*	1.5 W cm^{-2}	5	57.0	[149]
$Ti_3C_2T_x$	Colloidal solution	PTT	*S. aureus*	1.28 W cm^{-2}	5	–	[151]
$Ti_3C_2T_x$/PVA	Hydrogel	PTT	*S. aureus*	1.5 W cm^{-2}	10	–	[148]
$Ti_3C_2T_x/Bi_2S_3$	Wound dressing	PTT/ROS generation	*S. aureus*	0.7 W cm^{-2}	10	–	[16]
$Ti_3C_2T_x$/Ag	Hydrogel	PTT/Ag^+ release	*S. aureus*	1.5 W cm^{-2}	15	–	[41]
Nb_2C/Titanium plate	Implant	PTT/ROS generation	*S. aureus*	0.7 W cm^{-2}	10	52	[150]

harmful microbial-free drinking water. Using Janus pomelo peel/MXenes as the photothermal center, Guan et al. [155] reported a low-cost and multifunctional steam generator with a hydrophobic top and hydrophilic bottom, ensuring efficient and stable water evaporation (Fig. 12a). It was found that there was no inhibition zone of *S. aureus* around Janus pomelo peel, while a bacteriostatic zone with a width of 4.8 mm is clearly observed around Janus pomelo peel/MXenes heterojunctions, indicating that Janus pomelo peel/MXenes composites possessed exceptional antibacterial activity during water evaporation (Fig. 12b). Furthermore, even after 50 cycles of simulated sunlight irradiation, a high-efficiency evaporation performance could be maintained. These interesting findings indicated that this cost-effective, environmentally friendly and sustainable photothermal sponge held the promise for large-scale wastewater treatment and purification. Besides the foam structure, Qu et al. [42] proposed a new strategy to construct a $Ti_3C_2T_x$/Au photothermal membrane with efficient water evaporation capacity and antimicrobial activity under solar light irradiation (Fig. 12c). After ten cycles, the evaporation efficiency and rate of $Ti_3C_2T_x$/Au membrane were still maintained at 83.63% and 2.664 kg m^{-2} h^{-1}, respectively, displaying their recyclable potentials (Fig. 12d, e). By using the membrane, interfacial water evaporation was significantly enhanced compared to the control group (Fig. 12f). In dark, $Ti_3C_2T_x$/Au membrane exhibited negligible antibacterial effect. In sharp contrast, it could effectively kill all bacteria under irradiation, and the authors attributed this phenomenon to the hot-zone formed at the air–water interface and enough sterilization time (Fig. 12g). In the antibacterial process, the primary ROS produced by $Ti_3C_2T_x$/Au was detected as $^1O_2$. The oxidative stress self-protection of bacterial cells was weakened by the presence of heat and $^1O_2$. In addition to the design of a new efficient photothermal evaporation strategy based on surface-modified $Ti_3C_2T_x$, this work also demonstrated the bactericidal potential of MXenes during water purification. Combining antibacterial agents with inherent bactericidal properties and MXenes into an integrated photothermal film is also a promising strategy. Liu et al. [44] reported a $Ti_3C_2T_x$/Ag/polyacrylonitrile nanofiber-based evaporator, in which the flexibility and foldability of the nanofiber membrane were achieved by electrospinning technology (Fig. 12h). The combination of $Ti_3C_2T_x$ and Ag nanoparticles resulted in broad-spectrum light absorption, efficient photothermal conversion, exceptional catalytic performance (Fig. 12i, j), as well as high antibacterial activity with 99.9% killing efficiency. This evaporator not only exhibited high structural flexibility, excellent performance, and multiple functions but also could achieve a maximum evaporation rate of 2.08 kg m^{-2} h^{-1} under one sun irradiation (Fig. 12k, l). In the long run, this flexible, biofouling-resistant and efficient nanofiber membrane may find practical application in wastewater treatment. To summarize, as shown in Table 5, MXenes-containing evaporators for solar-driven water evaporation and purification have exhibited various

https://doi.org/10.1007/s40820-022-00901-w

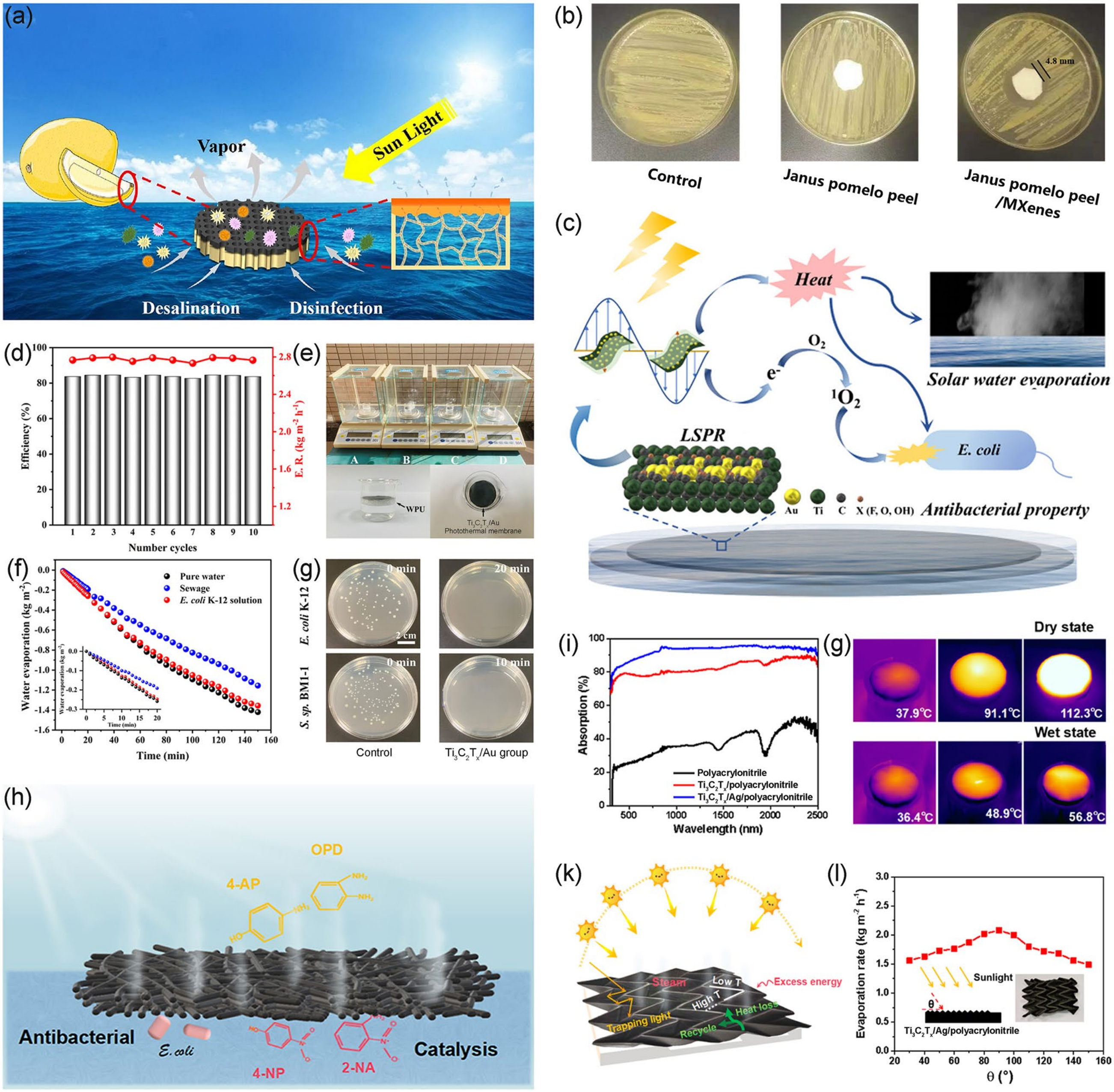

Fig. 12 **a** Schematic illustration of water evaporation and antibacterial property of Janus pomelo peel/MXenes; **b** Photographs of diffusion inhibition zone tests [155]. Copyright 2021 Elsevier. **c** Schematic illustration of solar water evaporation and antibacterial property of $Ti_3C_2T_x$/Au photothermal membrane; **d** Solar evaporation rate (right axis) and the corresponding evaporation efficiency (left axis) of $Ti_3C_2T_x$/Au photothermal membrane over 10 cycles (each cycle sustained over 1 h); **e** Photograph of the evaporation devices (A: control group, B: pure water, C: sewage from the Pearl River, D: *E. coli* K-12 solution); **f** Water evaporation performance of different solution systems; **g** Colony-forming units images of different bacteria after treatment with $Ti_3C_2T_x$/Au photothermal membrane under irradiation [42]. Copyright 2021, American Chemical Society. **h** Schematic illustration of water evaporation and antibacterial property of $Ti_3C_2T_x$/Ag/polyacrylonitrile nanofiber membrane; **i** Ultraviolet–visible–near-infrared (UV–vis–NIR) absorption spectra in the wavelength range from 300 to 2500 nm; **g** IR thermal images in the dry and wet state, the left column is polyacrylonitrile nanofiber membrane, the middle column is $Ti_3C_2T_x$/polyacrylonitrile nanofiber membrane, and the right column is $Ti_3C_2T_x$/Ag/polyacrylonitrile nanofiber membrane; **k** Schematic illustration of evaporator under different incident angles of sunlight; **l** Evaporation rate of fabricated $Ti_3C_2T_x$/Ag/polyacrylonitrile nanofiber-based origami evaporator under different incident angles of sunlight [44]. Copyright 2021, Elsevier

Table 5 Summary of antibacterial applications using MXenes-containing evaporators

Main components	Evaporator strategy	Antibacterial mechanisms	Bacteria	Antibacterial effect	Water evaporation rate (kg m^{-2} h^{-1})	References
$Ti_3C_2T_x$/Au/ polyvinylidene fluoride	A superior interface photothermal conversion material to achieve efficient evaporation and antibacterial properties	PTT/ROS generation	*E. coli* K-12	100%	2.66^a	[42]
			Spingopyxis sp. BM1-1	100%		
$Ti_3C_2T_x$/Ag/ polyacrylonitrile	A evaporator promising for practical clean water production	Physical damage/Ag^+ release	*E. coli*	100%	2.08^b	[44]
$Ti_3C_2T_x$/cellulose	A flexible anti-biofouling fibrous photothermal membrane	Physical damage	*E. coli*	99.9%	1.44^b	[152]
			S. aureus	99.9%		
$Ti_3C_2T_x$/ dimethylsiloxane/ hydrophilic polylactic acid/TiO_2	A flexible MXene-based Janus porous fibrous membranes for solar-driven desalination and antibacterial properties	Physical damage	*E. coli*	100%	1.0^b	[156]

^{a}2 sun illumination; ^{b}1 sun illumination

successful cases, shining light on practical applications in long-term water treatments.

4.4 Flexible Antibacterial Textiles

Smart flexible electronic devices, such as wearable sensors, medical monitoring devices and soft robots, have raised extensive public interest [36, 43, 49]. As well as their comfort and skin-friendliness, textile materials are breathable and flexible, making them an excellent option for flexible wearable devices. Nevertheless, achieving the multifunctional properties while maintaining the intrinsic advantages of the fabrics is still challenging. Since MXenes with layered structures exhibit unique surface chemical properties and comparable electrical conductivity to metals, they have been widely applied for fabricating flexible smart fabrics through dip coating and spray coating approaches [157, 158]. Yan et al. [45] reported the preparation of MXenes-decorated silk fabric with satisfying UV protection performance, electrothermal conversion capability and photothermal antibacterial property through in-situ dip-coating $Ti_3C_2T_x$ nanosheets onto silk fabric (Fig. 13a). Under continuous irradiation, the surface temperature of the fabric sample increased linearly, reached a saturation temperature within 100 s, and remained stable until the light was turned off (Fig. 13b). The rapid light response and stable photothermal conversion of this silk fabric also endowed it with high antibacterial capacity. Upon exposure to light irradiation for 20 min, the experimental group attained a 99.5% antibacterial efficiency (Fig. 13c). At the same time, the fabric of MXenes-containing silk still possessed skin-friendly properties, such as breathability and flexibility. Yan et al. [141] also designed a MXenes-based cotton fabric with micro breathing monitoring and rapid-photothermal antibacterial capabilities (Fig. 13d). Through electrostatic self-assembly, MXenes nanosheets and chitosan quaternary ammonium salt (HACC) strongly interacted while retaining the original breathability and softness of the cotton fabric. Based on the frequency and breathing depth of users, the cotton fabric could accurately monitor physiological health activities. This cotton

https://doi.org/10.1007/s40820-022-00901-w

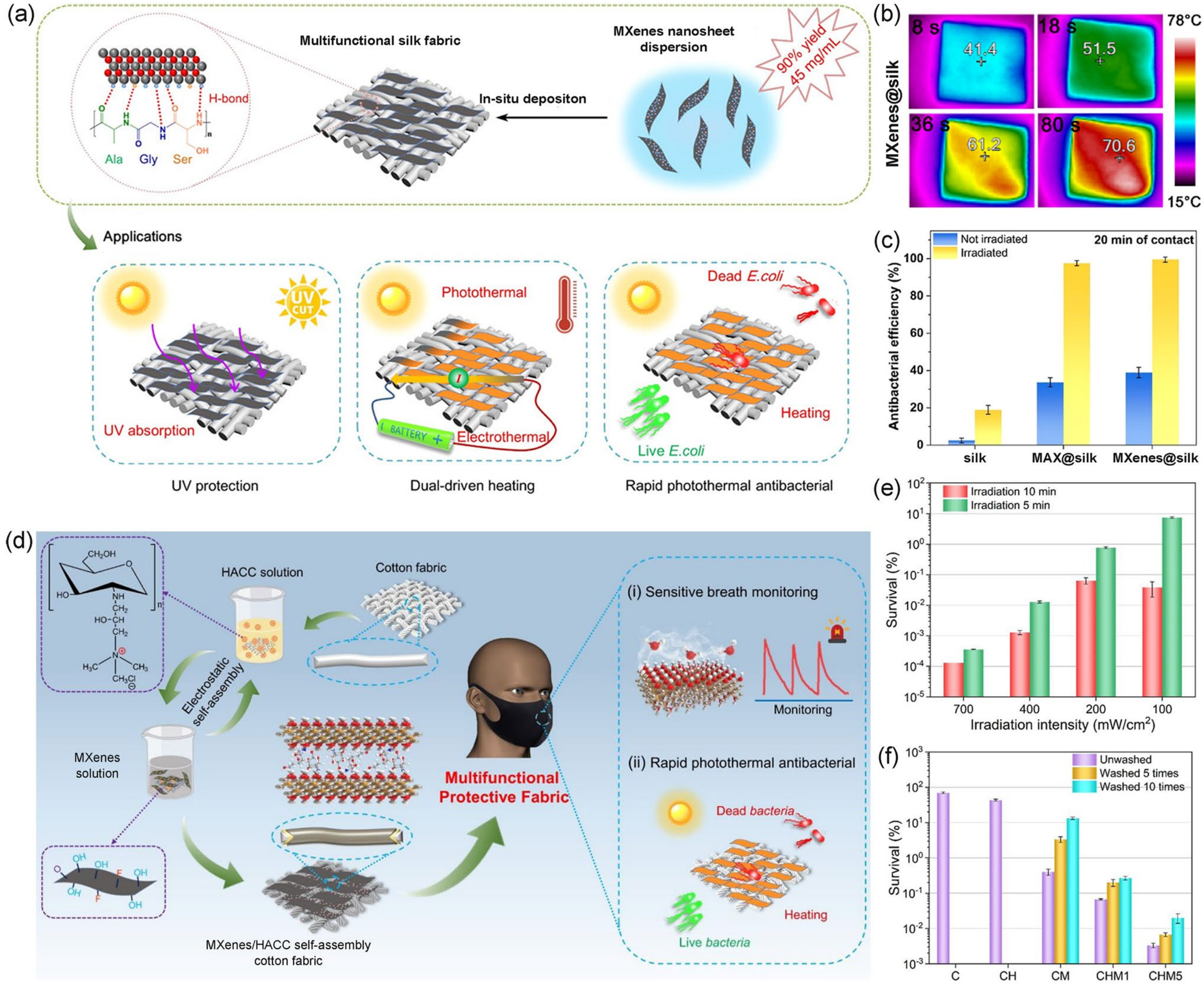

Fig. 13 **a** Schematic illustration of preparation and derivative functions of MXenes-based multifunctional silk fabric; **b** IR thermal images of the MXenes@silk; **c** The antibacterial efficiency of the different samples contacted for 20 min [45]. Copyright 2021, American Chemical Society. **d** Schematic illustration of preparation and application of multifunctional protective MXenes/HACC cotton fabric; **e** Antibacterial activity with different irradiation intensity and time; **f** Inactivation of fabric samples against *E. coli* and *S. aureus* before and after washing [141]. Copyright 2022, American Chemical Society

fabric also showed promising photothermal conversion ability, washing resistance and cycling stability. Furthermore, the fabric showed an antibacterial efficiency of nearly 100% against *E. coli* and *S. aureus* within 5 min under irradiation with the intensity of 400 mW cm^{-2} (Fig. 13e). Moreover, the antibacterial efficiency against both bacteria was still higher than 99% after being washed for ten times, indicating broad-spectrum photothermal antibacterial ability and stable repeatability (Fig. 13f). Similarly, as summarized in Table 6, MXenes-based multifunctional fabrics such as wearable electronics, self-disinfecting textiles, anti-infection treatment platforms, and textile coating have been successfully practised, showing a promising application prospect.

Table 6 Summary of photothermal-derived antibacterial applications using MXenes-containing fabrics

Main components	Fabric strategy	Antibacterial mechanisms	Light source	Bacteria	Effect	References
$Ti_3C_2T_x$/PDA[a]/Ni^{2+}	A knittable and sewable spandex yarn with conductive nacre-mimetic composite coating	Physical damage/PTT	808 nm, 2.0 W cm^{-2}	*E. coli*	99.9%	[46]
$Ti_3C_2T_x$/PCN-224 MOFs[b]	A smart photothermochromic self-disinfecting textile material	PTT/ROS generation	Xe lamp, 500 W, λ ≥ 420 nm, 15 cm distance	*E. coli*	99.9%	[157]
				S. aureus	99.9%	
$Ti_3C_2T_x$/Chitosan quaternary ammonium salt	A smart wearable multifunctional protective cotton fabric	PTT	Xe lamp, 0.4 W cm^{-2}	*E. coli*	100%	[157]
				S. aureus	100%	
$Ti_3C_2T_x$	A multifunctional heating fabric based on natural fiber	PTT	Xe lamp, 0.4 W cm^{-2}	*E. coli*	99.6%	[45]
$Ti_3C_2T_x$/Zeolite imidazole framework-8/Polylactic acid	A stimuli-responsive multifunctional electrospinning membrane	PTT/ROS generation	808 nm, 1.5 W cm^{-2}	*E. coli*	100%	[159]
				Methicillin-resistant *Staphylococcus aureus*	100%	
$Ti_3C_2T_x$/MoO_{3-x} quantum dots	A washable antibacterial polyester fabric	ROS generation	Sunlight	*E. coli*	~99%	[160]
				S. aureus	~99%	

[a]PDA: polydopamine; [b]PCN-224 MOFs: porous coordination network metal–organic frameworks

5 Conclusions and Perspectives

5.1 Conclusions

As summarized in this review, the past decade witnessed rapid progress in unlocking the potential applications of MXenes-based materials in antibacterial and related fields. From the diverse synthetic strategies to microstructure examinations, we have gained basic knowledge of the nature of this family of alluring materials. Benefiting from their intrinsic photothermal or photodynamic ability, MXenes can be directly utilized as PTAs or PSs presenting great application potential in the rapid sterilization and disinfection. Hyperthermia generated by MXenes due to photo-to-thermal conversion could inactivate the bioactive matrix such as proteins and polysaccharides in microbial cells, causing the inactivation of pathogenic cells. Moreover, multitudinous active sites of MXenes make various modifications feasible; for instance, heterojunction construction could effectively postpone the recombination of electrons and holes, thus promoting ROS generation. To date, plentiful creative and elaborate designs have been implemented in the applications of antibacterial and related fields, indicating the thriving potential of MXenes in the post-antibiotic era.

5.2 Challenges and Perspectives

Despite rigorous research and significant accomplishments so far, numerous fundamental issues remain unresolved. We have compiled a list of concerns that need to be addressed in order to push this field forward:

(1) Primarily, from the standpoint of green and safe synthesis, the use of fluorine-containing etchants, which is present in the most commonly used preparation process, poses a significant risk to the environment and

even to the health of researchers. And the subsequent treatment of waste liquid must meet stringent standards to fulfill the criterion for safe disposal handling. The novel preparation methods reported by using other fluorine-free reagents or reaction systems have received a lot of attention; however, it is not adaptable to a wide range of applications.

Therefore, the advanced preparation methods of MXenes are needed to realize practical applications. Experimentally, new etchants and intercalants, for a feasible MXene synthesis protocol, to achieve desired termination groups on the surface of MXenes and finely tuned properties are necessary to be explored.

(2) Since research into photothermal MXenes is still in its early stages, the mechanism of photo-to-thermal conversion is not fully understood. The absence of studies of interrelated issues makes the practical design of MXenes challenging.

Due to the chemical versatility of MXenes, more in-depth research and understanding of the photothermal mechanism is urgently needed, and developing a data pool of versatile MXenes, including full absorption spectra, temperature changes against optical power density, temperature evolution against time, the effects of synthetic protocols on photothermal performance and the general rules for optimizing photothermal performance will be beneficial.

(3) On account of the extremely high specific surface area, 2D materials with poor thermal stability are impressionable to the environment, among which MXenes are the sensitive ones in this category. MXenes can be readily decomposed to produce the oxides due to the synergistic contributions from air, moisture, and light. In practical applications, the stability of MXenes is of critical importance to ensure excellent photo-to-thermal conversion ability and effective antibacterial behaviors.

Thus, exploring and understanding the oxidation kinetics of MXenes is of great significance in predicting their changes in composition and performance over time. Besides, given that the oxidation of MXenes primitively occurs on the edges, passivating the edges via stable oxides or impervious materials can be considered.

(4) Photothermal-derived synergistic antibacterial therapy has emerged in the recent few decades, and the antibacterial mechanisms on MXenes need to be better established. Generally, an important attribute of bacterial inactivation is the damage to protective membrane structure which further leads to intracellular disturbance of homeostasis. There have been many efforts to verify the particular structure and processes whose alteration, under exposure to hyperthermia, causes bacteria death. Nonetheless, given the ambiguous and intricate interrelationships between the diverse structures and cellular functions, comprehension of experimental results is confused.

In this regard, systematic biological characterization is urgently needed to grasp the microscopic alteration of the critical component such as the outer and inner membrane, peptidoglycan cell wall, nucleoid, DNA, RNA, ribosomes, and diverse enzymes as well as the underlying structure-property relationships.

(5) Phototherapy itself still has several limitations, such as unitary treatment mode, local high power and high concentration requirements, and uncertain biocompatibility.

Hence, photothermal-derived synergistic strategies may need to be combined with other therapies, including but not limited to pharmacotherapy, chemotherapy, immunotherapy, starvation therapy and radiotherapy. For the selection of appropriate light power, imaging guidance is a befitting auxiliary to monitor the distribution of therapeutic agents to guide milder phototherapy.

(6) Another scruple is that biocompatibility is a pivotal issue in the therapeutic process. The cognition of the long-term effects on human health and the mechanisms of cytotoxicity is still insufficient. Although several remarkable achievements have been made in the in vivo treatments and short-term safety has been confirmed in these studies, more research and evaluations are essential to examine their long-term biosafety. Meanwhile, the potential impact of the degradation products is also necessary to be taken into consideration, which may lead to bioaccumulation and tissue toxicity.

To solve these issues, the computational simulation might be introduced to partly calculate the transformation of therapeutic agents and estimate the probable effects on healthy cells.

Acknowledgements This work was supported by the National Natural Science Foundation of China (21902085,51572157 and 82002793), the Natural Science Foundation of Shandong Province (ZR2019QF012, ZR2020QH183 and ZR2019BEM024), Shenzhen Fundamental Research Program (JCYJ20190807093205660 and JCYJ20190807092803583), and the fund of the State Key Laboratory of Solidification Processing in NWPU (SKLSP202108).

Funding Open access funding provided by Shanghai Jiao Tong University.

References

1. M. Tavakolian, S.M. Jafari, T.G.M. Ven, A review on surface-functionalized cellulosic nanostructures as biocompatible antibacterial materials. Nano-Micro Lett. **12**, 73 (2020). https://doi.org/10.1007/s40820-020-0408-4
2. J. Huo, Q. Jia, H. Huang, J. Zhang, P. Li et al., Emerging photothermal-derived multimodal synergistic therapy in combating bacterial infections. Chem. Soc. Rev. **50**(15), 8762–8789 (2021). https://doi.org/10.1039/d1cs00074h
3. Y. Li, D. Wang, J. Wen, P. Yu, J. Liu et al., Chemically grafted nanozyme composite cryogels to enhance antibacterial and biocompatible performance for bioliquid regulation and adaptive bacteria trapping. ACS Nano **15**(12), 19672–19683 (2021). https://doi.org/10.1021/acsnano.1c06983
4. L. Karner, S. Drechsler, M. Metzger, P. Slezak, J. Zipperle et al., Contamination of wounds with fecal bacteria in immuno-suppressed mice. Sci. Rep. **10**, 11494 (2020). https://doi.org/10.1038/s41598-020-68323-5
5. H. Gao, C. Cui, L. Wang, M. Jacobs-Lorena, S. Wang, Mosquito microbiota and implications for disease control. Trends Parasitol. **36**(2), 98–111 (2020). https://doi.org/10.1016/j.pt.2019.12.001
6. N.N. Dinh, H. Sze-Fui, H.M. Thi, N.V. Thi, R. Rees et al., Domestic dogs are mammalian reservoirs for the emerging zoonosis flea-borne spotted fever, caused by Rickettsia felis. Sci. Rep. **10**, 4151 (2020). https://doi.org/10.1038/s41598-020-61122-y
7. F.G.B. Goddard, H.H. Chang, T.F. Clasen, J.A. Sarnat, Exposure measurement error and the characterization of child exposure to fecal contamination in drinking water. Npj Clean Water **3**, 19 (2020). https://doi.org/10.1038/s41545-020-0063-9
8. H. Xu, Z. Chen, X. Wu, L. Zhao, N. Wang et al., Antibiotic contamination amplifies the impact of foreign antibiotic-resistant bacteria on soil bacterial community. Sci. Total Environ. **758**, 143693 (2021). https://doi.org/10.1016/j.scitotenv.2020.143693
9. Y. Huang, D. Xu, L. Huang, Y. Lou, J. Muhadesi et al., Responses of soil microbiome to steel corrosion. Npj Biofilms Microbio. **7**, 6 (2021). https://doi.org/10.1038/s41522-020-00175-3
10. H. Han, J. Yang, X. Li, Y. Qi, Z. Yang et al., Shining light on transition metal sulfides: new choices as highly efficient antibacterial agents. Nano Res. **14**(8), 2512–2534 (2021). https://doi.org/10.1007/s12274-021-3293-3
11. Y. Wang, Y. Jin, W. Chen, J. Wang, H. Chen et al., Construction of nanomaterials with targeting phototherapy properties to inhibit resistant bacteria and biofilm infections. Chem. Eng. J. **358**, 74–90 (2019). https://doi.org/10.1016/j.cej.2018.10.002
12. D.I. Andersson, D. Hughes, Antibiotic resistance and its cost: is it possible to reverse resistance? Nat. Rev. Microbiol. **8**(4), 260–271 (2010). https://doi.org/10.1038/nrmicro2319
13. Y. Zhang, X. Xie, W. Ma, Y. Zhan, C. Mao et al., Multi-targeted antisense oligonucleotide delivery by a framework nucleic acid for inhibiting biofilm formation and virulence. Nano-Micro Lett. **12**, 74 (2020). https://doi.org/10.1007/s40820-020-0409-3
14. Y. Song, Q. Sun, J. Luo, Y. Kong, B. Pan et al., Cationic and anionic antimicrobial agents co-templated mesostructured silica nanocomposites with a spiky nanotopology and enhanced biofilm inhibition performance. Nano-Micro Lett. **14**, 83 (2022). https://doi.org/10.1007/s40820-022-00826-4
15. H.C. Flemming, J. Wingender, U. Szewzyk, P. Steinberg, S.A. Rice et al., Biofilms: an emergent form of bacterial life. Nat. Rev. Microbiol. **14**(9), 563–575 (2016). https://doi.org/10.1038/nrmicro.2016.94
16. J. Li, Z. Li, X. Liu, C. Li, Y. Zheng et al., Interfacial engineering of $Bi_2S_3/Ti_3C_2T_x$ MXene based on work function for rapid photo-excited bacteria-killing. Nat. Commun. **12**, 1224 (2021). https://doi.org/10.1038/s41467-021-21435-6
17. Q. Wu, L. Tan, X. Liu, Z. Li, Y. Zhang et al., The enhanced near-infrared photocatalytic and photothermal effects of MXene-based heterojunction for rapid bacteria-killing. Appl. Catal. B **297**, 120500 (2021). https://doi.org/10.1016/j.apcatb.2021.120500
18. X. Cai, J. Tian, J. Zhu, J. Chen, L. Li et al., Photodynamic and photothermal co-driven CO-enhanced multi-mode synergistic antibacterial nanoplatform to effectively fight against biofilm infections. Chem. Eng. J. **426**, 131919 (2021). https://doi.org/10.1016/j.cej.2021.131919
19. J.M.A. Blair, M.A. Webber, A.J. Baylay, D.O. Ogbolu, L.J.V. Piddock, Molecular mechanisms of antibiotic resistance. Nat. Rev. Microbiol. **13**, 42–51 (2015). https://doi.org/10.1038/nrmicro3380

20. N. Thuy-Khanh, H.T.T. Duong, R. Selvanayagam, C. Boyer, N. Barraud, Iron oxide nanoparticle-mediated hyperthermia stimulates dispersal in bacterial biofilms and enhances antibiotic efficacy. Sci. Rep. **5**, 18385 (2015). https://doi.org/10.1038/srep18385
21. T. Wang, Z. Bai, W. Wei, F. Hou, W. Guo et al., β-cyclodextrin-derivative-functionalized graphene oxide/graphitic carbon nitride composites with a synergistic effect for rapid and efficient sterilization. ACS Appl. Mater. Interfaces **14**(1), 474–483 (2022). https://doi.org/10.1021/acsami.1c24047
22. X. Zhou, Z. Wang, Y.K. Chan, Y. Yang, Z. Jiao et al., Infection micromilieu-activated nanocatalytic membrane for orchestrating rapid sterilization and stalled chronic wound regeneration. Adv. Funct. Mater. **32**(7), 2109469 (2021). https://doi.org/10.1002/adfm.202109469
23. H. Han, X. Xu, H. Kan, Y. Tang, C. Liu et al., Synergistic photodynamic/photothermal bacterial inactivation over heterogeneous quaternized chitosan/silver/cobalt phosphide nanocomposites. J. Colloid Interface Sci. **616**, 304–315 (2022). https://doi.org/10.1016/j.jcis.2022.02.068
24. Q. Zhao, J. Wang, C. Yin, P. Zhang, J. Zhang et al., Near-infrared light-sensitive nano neuro-immune blocker capsule relieves pain and enhances the innate immune response for necrotizing infection. Nano Lett. **19**(9), 5904–5914 (2019). https://doi.org/10.1021/acs.nanolett.9b01459
25. C. Liu, W. Wang, M. Zhang, C. Zhang, C. Ma et al., Synthesis of MXene/COF/Cu_2O heterojunction for photocatalytic bactericidal activity and mechanism evaluation. Chem. Eng. J. **430**, 132663 (2022). https://doi.org/10.1016/j.cej.2021.132663
26. D. Wang, H. Wang, L. Ji, M. Xu, B. Bai et al., Hybrid plasmonic nanodumbbells engineering for multi-intensified second near-infrared light induced photodynamic therapy. ACS Nano **15**(5), 8694–8705 (2021). https://doi.org/10.1021/acsnano.1c00772
27. Y. Yang, X. Zhou, Y.K. Chan, Z. Wang, L. Li et al., Photo-activated nanofibrous membrane with self-rechargeable antibacterial function for stubborn infected cutaneous regeneration. Small **18**(12), 2105988 (2022). https://doi.org/10.1002/smll.202105988
28. Z. Yu, L. Jiang, R. Liu, W. Zhao, Z. Yang et al., Versatile self-assembled MXene-Au nanocomposites for SERS detection of bacteria, antibacterial and photothermal sterilization. Chem. Eng. J. **426**, 131914 (2021). https://doi.org/10.1016/j.cej.2021.131914
29. Y. Liang, H. Zhang, H. Yuan, W. Lu, Z. Li et al., Conjugated polymer and triphenylamine derivative codoped nanoparticles for photothermal and photodynamic antimicrobial therapy. ACS Appl. Bio Mater. **3**(6), 3494–3499 (2020). https://doi.org/10.1021/acsabm.0c00320
30. Y. Yang, Y. Deng, J. Huang, X. Fan, C. Cheng et al., Size-transformable metal-organic framework-derived nanocarbons for localized chemo-photothermal bacterial ablation and wound disinfection. Adv. Funct. Mater. **29**(33), 1900143 (2019). https://doi.org/10.1002/adfm.201900143
31. J.B. Pang, R.G. Mendes, A. Bachmatiuk, L. Zhao, H.Q. Ta et al., Applications of 2D MXenes in energy conversion and storage systems. Chem. Soc. Rev. **48**(1), 72–133 (2019). https://doi.org/10.1039/c8cs00324f
32. S. Cao, B. Shen, T. Tong, J. Fu, J. Yu, 2D/2D heterojunction of ultrathin MXene/Bi_2WO_6 nanosheets for improved photocatalytic CO_2 reduction. Adv. Funct. Mater. **28**(21), 1800136 (2018). https://doi.org/10.1002/adfm.201800136
33. M. Naguib, V.N. Mochalin, M.W. Barsoum, Y. Gogotsi, 25th anniversary article: MXenes: a new family of two-dimensional materials. Adv. Mater. **26**(7), 992–1005 (2014). https://doi.org/10.1002/adma.201304138
34. E.A. Hussein, M.M. Zagho, B.R. Rizeq, N.N. Younes, G. Pintus et al., Plasmonic MXene-based nanocomposites exhibiting photothermal therapeutic effects with lower acute toxicity than pure MXene. Int. J. Nanomed. **14**, 4529–4539 (2019). https://doi.org/10.2147/ijn.S202208
35. A.V. Mohammadi, J. Rosen, Y. Gogotsi, The world of two-dimensional carbides and nitrides (MXenes). Science **372**(6547), abf1581 (2021). https://doi.org/10.1126/science.abf1581
36. Z. Xiang, Y. Shi, X. Zhu, L. Cai, W. Lu, Flexible and waterproof 2D/1D/0D construction of MXene-based nanocomposites for electromagnetic wave absorption, EMI shielding, and photothermal conversion. Nano-Micro Lett. **13**, 150 (2021). https://doi.org/10.1007/s40820-021-00673-9
37. F. Wu, H. Zheng, W. Wang, Q. Wu, Q. Zhang et al., Rapid eradication of antibiotic-resistant bacteria and biofilms by MXene and near-infrared light through photothermal ablation. Sci. China Mater. **64**(3), 748–758 (2021). https://doi.org/10.1007/s40843-020-1451-7
38. G. Liu, J. Zou, Q. Tang, X. Yang, Y. Zhang et al., Surface modified Ti_3C_2 MXene nanosheets for tumor targeting photothermal/photodynamic/chemo synergistic therapy. ACS Appl. Mater. Interfaces **9**(46), 40077–40086 (2017). https://doi.org/10.1021/acsami.7b13421
39. Y. Liu, Y. Tian, Q. Han, J. Yin, J. Zhang et al., Synergism of 2D/1D MXene/cobalt nanowire heterojunctions for boosted photo-activated antibacterial application. Chem. Eng. J. **410**, 128209 (2021). https://doi.org/10.1016/j.cej.2020.128209
40. Y. Zheng, Y. Yan, L. Lin, Q. He, H. Hu et al., Titanium carbide MXene-based hybrid hydrogel for chemo-photothermal combinational treatment of localized bacterial infection. Acta Biomater. **142**, 113–123 (2022). https://doi.org/10.1016/j.actbio.2022.02.019
41. X. Zhu, Y. Zhu, K. Jia, B.S. Abraha, Y. Li et al., A near-infrared light-mediated antimicrobial based on Ag/$Ti_3C_2T_x$for effective synergetic antibacterial applications. Nanoscale **12**(37), 19129–19141 (2020). https://doi.org/10.1039/d0nr04925e
42. W. Qu, H. Zhao, Q. Zhang, D. Xia, Z. Tang et al., Multifunctional Au/Ti_3C_2 photothermal membrane with antibacterial ability for stable and efficient solar water purification under the full spectrum. ACS Sustain. Chem. Eng. **9**(34), 11372–11387 (2021). https://doi.org/10.1021/acssuschemeng.1c03096

43. Y. Zhang, J.K. El-Demellawi, Q. Jiang, G. Ge, H. Liang et al., MXene hydrogels: fundamentals and applications. Chem. Soc. Rev. **49**(20), 7229–7251 (2020). https://doi.org/10.1039/d0cs00022a
44. H. Liu, Y. Liu, L. Wang, X. Qin, J. Yu, Nanofiber-based origami evaporator for multifunctional and omnidirectional solar steam generation. Carbon **177**, 199–206 (2021). https://doi.org/10.1016/j.carbon.2021.02.081
45. B. Yan, M. Zhou, X. Liao, P. Wang, Y. Yu et al., Developing a multifunctional silk fabric with dual-driven heating and rapid photothermal antibacterial abilities using high-yield MXene dispersions. ACS Appl. Mater. Interfaces **13**(36), 43414–43425 (2021). https://doi.org/10.1021/acsami.1c12915
46. M. Gong, L. Yue, J. Kong, X. Lin, L. Zhang et al., Knittable and sewable spandex yarn with nacre-mimetic composite coating for wearable health monitoring and thermo- and antibacterial therapies. ACS Appl. Mater. Interfaces **13**(7), 9053–9063 (2021). https://doi.org/10.1021/acsami.1c00864
47. R.P. Pandey, P.A. Rasheed, T. Gomez, K. Rasool, J. Ponraj et al., Effect of sheet size and atomic structure on the antibacterial activity of Nb-MXene nanosheets. ACS Appl. Nano Mater. **3**(11), 11372–11382 (2020). https://doi.org/10.1021/acsanm.0c02463
48. H. Feng, W. Wang, M. Zhang, S. Zhu, Q. Wang et al., 2D titanium carbide-based nanocomposites for photocatalytic bacteriostatic applications. Appl. Catal. B **266**, 118609 (2020). https://doi.org/10.1016/j.apcatb.2020.118609
49. Y. Pei, X. Zhang, Z. Hui, J. Zhou, X. Huang et al., $Ti_3C_2T_X$ MXene for sensing applications: recent progress, design principles, and future perspectives. ACS Nano **15**(3), 3996–4017 (2021). https://doi.org/10.1021/acsnano.1c00248
50. A. Guo, X. Zhang, S. Wang, J. Zhu, L. Yang et al., Excellent microwave absorption and electromagnetic interference shielding based on reduced graphene oxide@MoS_2/poly(vinylidene fluoride) composites. ChemPlusChem **81**(12), 1305–1311 (2016). https://doi.org/10.1002/cplu.201600370
51. M. Naguib, M. Kurtoglu, V. Presser, J. Lu, J. Niu et al., Two-dimensional nanocrystals produced by exfoliation of Ti_3AlC_2. Adv. Mater. **23**(37), 4248–4253 (2011). https://doi.org/10.1002/adma.201102306
52. M. Alhabeb, K. Maleski, B. Anasori, P. Lelyukh, L. Clark et al., Guidelines for synthesis and processing of two-dimensional titanium carbide ($Ti_3C_2T_X$ MXene). Chem. Mater. **29**(18), 7633–7644 (2017). https://doi.org/10.1021/acs.chemmater.7b02847
53. B. Deng, Z. Liu, F. Pan, Z. Xiang, X. Zhang et al., Electrostatically self-assembled two-dimensional magnetized MXene/hollow Fe_3O_4 nanoparticle hybrids with high electromagnetic absorption performance and improved impendence matching. J. Mater. Chem. A **9**(6), 3500–3510 (2021). https://doi.org/10.1039/d0ta10551a
54. Y.J. Kim, S.J. Kim, D. Seo, Y. Chae, M. Anayee et al., Etching mechanism of monoatomic aluminum layers during MXene synthesis. Chem. Mater. **33**(16), 6346–6355 (2021). https://doi.org/10.1021/acs.chemmater.1c01263
55. F. Liu, A. Zhou, J. Chen, J. Jin, W. Zhou et al., Preparation of Ti_3C_2 and Ti_2C MXenes by fluoride salts etching and methane adsorptive properties. Appl. Surf. Sci. **416**, 781–789 (2017). https://doi.org/10.1016/j.apsusc.2017.04.239
56. R. Zhao, H. Di, C. Wang, X. Hui, D. Zhao et al., Encapsulating ultrafine Sb nanoparticles in Na^+ pre-intercalated 3D porous $Ti_3C_2T_X$ MXene nanostructures for enhanced potassium storage performance. ACS Nano **14**(10), 13938–13951 (2020). https://doi.org/10.1021/acsnano.0c06360
57. C.F. Zhang, S.N. Park, A. Seral-Ascaso, S. Barwich, N. McEyoy et al., High capacity silicon anodes enabled by MXene viscous aqueous ink. Nat. Commun. **10**, 849 (2019). https://doi.org/10.1038/s41467-019-08383-y
58. C.F. Zhang, B. Anasori, A. Seral-Ascaso, S.H. Park, N. McEvoy et al., Transparent, flexible, and conductive 2D titanium carbide (MXene) films with high volumetric capacitance. Adv. Mater. **29**(36), 1702678 (2017). https://doi.org/10.1002/adma.201702678
59. F. Du, H. Tang, L.M. Pan, T. Zhang, H.M. Lu et al., Environmental friendly scalable production of colloidal 2D titanium carbonitride MXene with minimized nanosheets restacking for excellent cycle life lithium-ion batteries. Electrochim. Acta **235**, 690–699 (2017). https://doi.org/10.1016/j.electacta.2017.03.153
60. M. Ghidiu, J. Halim, S. Kota, D. Bish, Y. Gogotsi et al., Ion-exchange and cation solvation reactions in Ti_3C_2 MXene. Chem. Mater. **28**(10), 3507–3514 (2016). https://doi.org/10.1021/acs.chemmater.6b01275
61. M. Ghidiu, M.R. Lukatskaya, M. Zhao, Y. Gogotsi, M.W. Barsoum, Conductive two-dimensional titanium carbide ‘clay’ with high volumetric capacitance. Nature **516**(7529), 78–81 (2014). https://doi.org/10.1038/nature13970
62. A. Feng, Y. Yu, Y. Wang, F. Jiang, Y. Yu et al., Two-dimensional MXene Ti_3C_2 produced by exfoliation of Ti_3AlC_2. Mater. Des. **114**, 161–166 (2017). https://doi.org/10.1016/j.matdes.2016.10.053
63. J. Halim, M.R. Lukatskaya, K.M. Cook, J. Lu, C.R. Smith et al., Transparent conductive two-dimensional titanium carbide epitaxial thin films. Chem. Mater. **26**(7), 2374–2381 (2014). https://doi.org/10.1021/cm500641a
64. K. Liang, A. Tabassum, A. Majed, C. Dun, F.P. Yang et al., Synthesis of new two-dimensional titanium carbonitride Ti2C0.5N0.5Tx MXene and its performance as an electrode material for sodium-ion battery. InfoMat **3**(12), 1422–1430 (2021). https://doi.org/10.1002/inf2.12269
65. H.T. He, Q.X. Xia, B.X. Wang, L.B. Wang, Q.K. Hu et al., Two-dimensional vanadium carbide (V_2CT_x) MXene as supercapacitor electrode in seawater electrolyte. Chin. Chem. Lett. **31**(4), 984–987 (2020). https://doi.org/10.1016/j.cclet.2019.08.025
66. M. Li, J. Lu, K. Luo, Y. Li, K. Chang et al., Element replacement approach by reaction with Lewis acidic molten salts to synthesize nanolaminated MAX phases and MXenes. J. Am.

Chem. Soc. **141**(11), 4730–4737 (2019). https://doi.org/10.1021/jacs.9b00574

67. Y. Li, H. Shao, Z. Lin, J. Lu, L. Liu et al., A general Lewis acidic etching route for preparing MXenes with enhanced electrochemical performance in non-aqueous electrolyte. Nat. Mater. **19**(8), 894–899 (2020). https://doi.org/10.1038/s41563-020-0657-0
68. C. Xu, L. Wang, Z. Liu, L. Chen, J. Guo et al., Large-area high-quality 2D ultrathin Mo_2C superconducting crystals. Nat. Mater. **14**(11), 1135–1141 (2015). https://doi.org/10.1038/nmat4374
69. D. Geng, X. Zhao, Z. Chen, W. Sun, W. Fu et al., Direct synthesis of large-area 2D Mo_2C on in situ grown graphene. Adv. Mater. **29**(35), 1700072 (2017). https://doi.org/10.1002/adma.201700072
70. L. Gao, C. Li, W. Huang, S. Mei, H. Lin et al., MXene/polymer membranes: synthesis, properties, and emerging applications. Chem. Mater. **32**(5), 1703–1747 (2020). https://doi.org/10.1021/acs.chemmater.9b04408
71. L. Verger, C. Xu, V. Natu, H. Cheng, W. Ren et al., Overview of the synthesis of MXenes and other ultrathin 2D transition metal carbides and nitrides. Curr. Opin. Solid State Mater. Sci. **23**(3), 149–163 (2019). https://doi.org/10.1016/j.cossms.2019.02.001
72. M. Naguib, O. Mashtalir, J. Carle, V. Presser, J. Lu et al., Two-dimensional transition metal carbides. ACS Nano **6**(2), 1322–1331 (2012). https://doi.org/10.1021/nn204153h
73. M. Alhabeb, K. Maleski, T.S. Mathis, A. Sarycheva, C.B. Hatter et al., Selective etching of silicon from Ti_3SiC_2 (MAX) To obtain 2D titanium carbide (MXene). Angew. Chem. Int. Ed. **57**(19), 5444–5448 (2018). https://doi.org/10.1002/anie.201802232
74. X.H. Sang, Y. Xie, M.W. Lin, M. Alhabeb, K.L.V. Aken et al., Atomic defects in monolayer titanium carbide ($Ti_3C_2T_x$) MXene. ACS Nano **10**(10), 9193–9200 (2016). https://doi.org/10.1021/acsnano.6b05240
75. B. Anasori, Y. Xie, M. Beidaghi, J. Lu, B.C. Hosler et al., Two-dimensional, ordered, double transition metals carbides (MXenes). ACS Nano **9**(10), 9507–9516 (2015). https://doi.org/10.1021/acsnano.5b03591
76. J. Halim, S. Kota, M.R. Lukatskaya, M. Naguib, M.Q. Zhao et al., Synthesis and characterization of 2D molybdenum carbide (MXene). Adv. Funct. Mater. **26**(18), 3118–3127 (2016). https://doi.org/10.1002/adfm.201505328
77. F.F. Liu, J. Zhou, S.W. Wang, B.X. Wang, C. Shen et al., Preparation of high-purity V_2C MXene and electrochemical properties as li-ion batteries. J. Electrochem. Soc. **164**(4), A709–A713 (2017). https://doi.org/10.1149/2.0641704jes
78. A. Rosenkranz, G. Perini, J.Y. Aguilar-Hurtado, D.F. Zambrano, B. Wang et al., Laser-mediated antibacterial effects of few- and multi-layer $Ti_3C_2T_x$ MXenes. Appl. Surf. Sci. **567**, 150795 (2021). https://doi.org/10.1016/j.apsusc.2021.150795
79. V.M.H. Ng, H. Huang, K. Zhou, P.S. Lee, W. Que et al., Recent progress in layered transition metal carbides and/or nitrides (MXenes) and their composites: synthesis and applications. J. Mater. Chem. A **5**(7), 3039–3068 (2017). https://doi.org/10.1039/c6ta06772g
80. Z. Xie, Y. Duo, Z. Lin, T. Fan, C. Xing et al., The rise of 2D photothermal materials beyond graphene for clean water production. Adv. Sci. **7**(5), 1902236 (2020). https://doi.org/10.1002/advs.201902236
81. R. Li, L. Zhang, L. Shi, P. Wang, MXene Ti_3C_2: an effective 2D light-to-heat conversion material. ACS Nano **11**(4), 3752–3759 (2017). https://doi.org/10.1021/acsnano.6b08415
82. J. Xuan, Z. Wang, Y. Chen, D. Liang, L. Cheng et al., Organic-base-driven intercalation and delamination for the production of functionalized titanium carbide nanosheets with superior photothermal therapeutic performance. Angew. Chem. Int. Ed. **55**(47), 14569–14574 (2016). https://doi.org/10.1002/anie.201606643
83. O. Mashtalir, M. Naguib, V.N. Mochalin, Y. Dall'Agnese, M. Heon et al., Intercalation and delamination of layered carbides and carbonitrides. Nat. Commun. **4**, 1716 (2013). https://doi.org/10.1038/ncomms2664
84. M. Naguib, R.R. Unocic, B.L. Armstrong, J. Nanda, Large-scale delamination of multi-layers transition metal carbides and carbonitrides "MXenes." Dalton Trans. **44**(20), 9353–9358 (2015). https://doi.org/10.1039/c5dt01247c
85. M. Soleymaniha, M.A. Shahbazi, A.R. Rafieerad, A. Maleki, A. Amiri, Promoting role of MXene nanosheets in biomedical sciences: therapeutic and biosensing innovations. Adv. Healthc. Mater. **8**(1), 1801137 (2019). https://doi.org/10.1002/adhm.201801137
86. F. Shahzad, M. Alhabeb, C.B. Hatter, B. Anasori, S.M. Hong et al., Electromagnetic interference shielding with 2D transition metal carbides (MXenes). Science **353**(6304), 1137–1140 (2016). https://doi.org/10.1126/science.aag2421
87. O. Mashtalir, M.R. Lukatskaya, A.I. Kolesnikov, E. Raymundo-Pinero, M. Naguib et al., The effect of hydrazine intercalation on the structure and capacitance of 2D titanium carbide (MXene). Nanoscale **8**(17), 9128–9133 (2016). https://doi.org/10.1039/c6nr01462c
88. H. Wang, J. Zhang, Y. Wu, H. Huang, G. Li et al., Surface modified MXene Ti_3C_2 multilayers by aryl diazonium salts leading to large-scale delamination. Appl. Surf. Sci. **384**, 287–293 (2016). https://doi.org/10.1016/j.apsusc.2016.05.060
89. J. Ran, G. Gao, F. Li, T. Ma, A. Du et al., Ti_3C_2 MXene co-catalyst on metal sulfide photo-absorbers for enhanced visible-light photocatalytic hydrogen production. Nat. Commun. **8**, 13907 (2017). https://doi.org/10.1038/ncomms13907
90. M.R. Lukatskaya, S. Kota, Z. Lin, M. Zhao, N. Shpigel et al., Ultra-high-rate pseudocapacitive energy storage in two-dimensional transition metal carbides. Nat. Energy **2**(8), 17105 (2017). https://doi.org/10.1038/nenergy.2017.105
91. X. Liang, A. Garsuch, L.F. Nazar, Sulfur cathodes based on conductive MXene nanosheets for high-performance lithium-sulfur batteries. Angew. Chem. Int. Ed. **54**(13), 3907–3911 (2015). https://doi.org/10.1002/anie.201410174
92. B. Anasori, M.R. Lukatskaya, Y. Gogotsi, 2D metal carbides and nitrides (MXenes) for energy storage. Nat. Rev. Mater.

2(2), 16098 (2017). https://doi.org/10.1038/natrevmats.2016.98

93. A. Lipatov, M. Alhabeb, M.R. Lukatskaya, A. Boson, Y. Gogotsi et al., Effect of synthesis on quality, electronic properties and environmental stability of individual monolayer Ti_3C_2 MXene flakes. Adv. Electron. Mater. **2**(12), 1600255 (2016). https://doi.org/10.1002/aelm.201600255
94. J.B. Pang, A. Bachmatiuk, I. Ibrahim, L. Fu, D. Placha et al., CVD growth of 1D and 2D sp^2 carbon nanomaterials. J. Mater. Sci. **51**(2), 640–667 (2016). https://doi.org/10.1007/s10853-015-9440-z
95. J.B. Pang, A. Bachmatiuk, L. Fu, C.L. Yan, M.Q. Zeng et al., Oxidation as a means to remove surface contaminants on cu foil prior to graphene growth by chemical vapor deposition. J. Phys. Chem. C **119**(23), 13363–13368 (2015). https://doi.org/10.1021/acs.jpcc.5b03911
96. V. Kamysbayev, A.S. Filatov, H. Hu, X. Rui, F. Lagunas et al., Covalent surface modifications and superconductivity of two-dimensional metal carbide MXenes. Science **369**(6506), 979–983 (2020). https://doi.org/10.1126/science.aba8311
97. M. Seredych, C.E. Shuck, D. Pinto, M. Alhabeb, E. Precetti et al., High-temperature behavior and surface chemistry of carbide MXenes studied by thermal analysis. Chem. Mater. **31**(9), 3324–3332 (2019). https://doi.org/10.1021/acs.chemmater.9b00397
98. M.A. Hope, A.C. Forse, K.J. Griffith, M.R. Lukatskaya, M. Ghidiu et al., NMR reveals the surface functionalisation of Ti_3C_2 MXene. Phys. Chem. Chem. Phys. **18**(7), 5099–5102 (2016). https://doi.org/10.1039/c6cp00330c
99. X.F. Wang, X. Shen, Y.R. Gao, Z.X. Wang, R.C. Yu et al., Atomic-scale recognition of surface structure and intercalation mechanism of Ti_3C_2X. J. Am. Chem. Soc. **137**(7), 2715–2721 (2015). https://doi.org/10.1021/ja512820k
100. J.L. Hart, K. Hantanasirisakul, A.C. Lang, B. Anasori, D. Pinto et al., Control of MXenes' electronic properties through termination and intercalation. Nat. Commun. **10**, 522 (2019). https://doi.org/10.1038/s41467-018-08169-8
101. I. Persson, J. Halim, T.W. Hansen, J.B. Wagner, V. Darakchieva et al., How much oxygen can a MXene surface take before it breaks? Adv. Funct. Mater. **30**(47), 1909005 (2020). https://doi.org/10.1002/adfm.201909005
102. Q. Tang, Z. Zhou, P. Shen, Are MXenes promising anode materials for li ion batteries? computational studies on electronic properties and li storage capability of Ti_3C_2 and $Ti_3C_2X_2$ ($X = F$, OH) monolayer. J. Am. Chem. Soc. **134**(40), 16909–16916 (2012). https://doi.org/10.1021/ja308463r
103. P. Srivastava, A. Mishra, H. Mizuseki, K.R. Lee, A.K. Singh, Mechanistic insight into the chemical exfoliation and functionalization of Ti_3C_2 MXene. ACS Appl. Mater. Interfaces **8**(36), 24256–24264 (2016). https://doi.org/10.1021/acsami.6b08413
104. K. Zheng, K. Li, T.H. Chang, J. Xie, P.Y. Chen, Synergistic antimicrobial capability of magnetically oriented graphene oxide conjugated with gold nanoclusters. Adv. Funct. Mater. **29**(46), 1904603 (2019). https://doi.org/10.1002/adfm.201904603
105. L. Mei, S. Zhu, W. Yin, C. Chen, G. Nie et al., Two-dimensional nanomaterials beyond graphene for antibacterial applications: current progress and future perspectives. Theranostics **10**(2), 757–781 (2020). https://doi.org/10.7150/thno.39701
106. D.B. Wang, Y.X. Fang, W. Yu, L.L. Wang, H.Q. Xie et al., Significant solar energy absorption of MXene $Ti_3C_2T_x$ nanofluids via localized surface plasmon resonance. Sol. Energy Mater. Sol. Cells **220**, 110850 (2021). https://doi.org/10.1016/j.solmat.2020.110850
107. K. Wen, H. Tan, Q. Peng, H. Chen, H. Ma et al., Achieving efficient NIR-II type-I photosensitizers for photodynamic/photothermal therapy upon regulating chalcogen elements. Adv. Mater. **34**(7), 2108146 (2022). https://doi.org/10.1002/adma.202108146
108. Y. Qiao, J. He, W. Chen, Y. Yu, W. Li et al., Light-activatable synergistic therapy of drug-resistant bacteria-infected cutaneous chronic wounds and nonhealing keratitis by cupriferous hollow nanoshells. ACS Nano **14**(3), 3299–3315 (2020). https://doi.org/10.1021/acsnano.9b08930
109. L. Zhu, M. Gao, C.K.N. Peh, G.W. Ho, Solar-driven photothermal nanostructured materials designs and prerequisites for evaporation and catalysis applications. Mater. Horiz. **5**(3), 323–343 (2018). https://doi.org/10.1039/c7mh01064h
110. D. Xu, Z. Li, L. Li, J. Wang, Insights into the photothermal conversion of 2D MXene nanomaterials: synthesis, mechanism, and applications. Adv. Funct. Mater. **30**(47), 2000712 (2020). https://doi.org/10.1002/adfm.202000712
111. X.Q. Fan, L. Liu, X. Jin, W.T. Wang, S.F. Zhang et al., MXene $Ti_3C_2T_x$ for phase change composite with superior photothermal storage capability. J. Mater. Chem. A **7**(23), 14319–14327 (2019). https://doi.org/10.1039/c9ta03962g
112. Z. Li, Y. Chen, Y. Sun, X. Zhang, Platinum-doped prussian blue nanozymes for multiwavelength bioimaging guided photothermal therapy of tumor and anti-inflammation. ACS Nano **15**(3), 5189–5200 (2021). https://doi.org/10.1021/acsnano.0c10388
113. T. He, C. Jiang, J. He, Y. Zhang, G. He et al., Manganese-dioxide-coating-instructed plasmonic modulation of gold nanorods for activatable duplex-imaging-guided NIR-II photothermal-chemodynamic therapy. Adv. Mater. **33**(13), 2008540 (2021). https://doi.org/10.1002/adma.202008540
114. J.M. Luther, P.K. Jain, T. Ewers, A.P. Alivisatos, Localized surface plasmon resonances arising from free carriers in doped quantum dots. Nat. Mater. **10**(5), 361–366 (2011). https://doi.org/10.1038/nmat3004
115. A.R. Mallah, M.N.M. Zubir, O.A. Alawi, K.M.S. Newaz, A.B.M. Badry, Plasmonic nanofluids for high photothermal conversion efficiency in direct absorption solar collectors: fundamentals and applications. Sol. Energy Mater. Sol. Cells **201**, 110084 (2019). https://doi.org/10.1016/j.solmat.2019.110084
116. V. Mauchamp, M. Bugnet, E.P. Bellido, G.A. Botton, P. Moreau et al., Enhanced and tunable surface plasmons in two-dimensional Ti_3C_2 stacks: electronic structure versus

boundary effects. Phys. Rev. B **89**(23), 235428 (2014). https://doi.org/10.1103/PhysRevB.89.235428

117. J.K. El-Demellawi, S. Lopatin, J. Yin, O.F. Mohammed, H.N. Alshareef, Tunable multipolar surface plasmons in 2D $Ti_3C_2T_X$ MXene flakes. ACS Nano **12**(8), 8485–8493 (2018). https://doi.org/10.1021/acsnano.8b04029
118. A.D. Dillon, M.J. Ghidiu, A.L. Krick, J. Griggs, S.J. May et al., Highly conductive optical quality solution-processed films of 2D titanium carbide. Adv. Funct. Mater. **26**(23), 4162–4168 (2016). https://doi.org/10.1002/adfm.201600357
119. X. Wu, J. Wang, Z. Wang, F. Sun, Y. Liu et al., Boosting the electrocatalysis of MXenes by plasmon-induced thermalization and hot-electron injection. Angew. Chem. Int. Ed. **60**(17), 9416–9420 (2021). https://doi.org/10.1002/anie.202016181
120. G. Cebrian, S. Condon, P. Manas, Physiology of the inactivation of vegetative bacteria by thermal treatments: mode of action, influence of environmental factors and inactivation kinetics. Foods **6**(12), 107 (2017). https://doi.org/10.3390/foods6120107
121. K. Rasool, M. Helal, A. Ali, C.E. Ren, Y. Gogotsi et al., Antibacterial activity of $Ti_3C_2T_x$ MXene. ACS Nano **10**(3), 3674–3684 (2016). https://doi.org/10.1021/acsnano.6b00181
122. A. Rafieerad, W. Yan, A. Amiri, S. Dhingra, Bioactive and trackable MXene quantum dots for subcellular nanomedicine applications. Mater. Des. **196**, 109091 (2020). https://doi.org/10.1016/j.matdes.2020.109091
123. J. Gou, L. Zhao, Y. Li, J. Zhang, Nitrogen-doped Ti_2C MXene quantum dots as antioxidants. ACS Appl. Nano Mater. **4**(11), 12308–12315 (2021). https://doi.org/10.1021/acsanm.1c02783
124. Q. Zhong, Y. Li, G. Zhang, Two-dimensional MXene-based and MXene-derived photocatalysts: recent developments and perspectives. Chem. Eng. J. **409**, 128099 (2021). https://doi.org/10.1016/j.cej.2020.128099
125. X. Yu, X. Cai, H. Cui, S.W. Lee, X.F. Yu et al., Fluorine-free preparation of titanium carbide MXene quantum dots with high near-infrared photothermal performances for cancer therapy. Nanoscale **9**(45), 17859–17864 (2017). https://doi.org/10.1039/c7nr05997c
126. M. Marcen, V. Ruiz, M.J. Serrano, S. Condon, P. Manas, Oxidative stress in E. coli cells upon exposure to heat treatments. Int. J. Food Microbiol. **241**, 198–205 (2017). https://doi.org/10.1016/j.ijfoodmicro.2016.10.023
127. B. Kramer, J. Thielmann, Monitoring the live to dead transition of bacteria during thermal stress by a multi-method approach. J. Microbiol. Methods **123**, 24–30 (2016). https://doi.org/10.1016/j.mimet.2016.02.009
128. I. Leguerinel, I. Spegagne, O. Couvert, L. Coroller, P. Mafart, Quantifying the effects of heating temperature, and combined effects of heating medium pH and recovery medium pH on the heat resistance of Salmonella typhimurium. Int. J. Food Microbiol. **116**(1), 88–95 (2007). https://doi.org/10.1016/j.ijfoodmicro.2006.12.016
129. S. Zamenhof, Gene unstabilization induced by heat and by nitrous acid. J. Bacteriol. **81**(1), 111–117 (1961). https://doi.org/10.1128/jb.81.1.111-117.1961
130. A. Schon, E. Freire, Reversibility and irreversibility in the temperature denaturation of monoclonal antibodies. Anal. Biochem. **626**, 114240 (2021). https://doi.org/10.1016/j.ab.2021.114240
131. C.J. Nelson, M.J. Laconte, B.E. Bowler, Direct detection of heat and cold denaturation for partial unfolding of a protein. J. Am. Chem. Soc. **123**(30), 7453–7454 (2001). https://doi.org/10.1021/ja016144a
132. X. Xu, M. Fan, Z. Yu, Y. Zhao, H. Zhang et al., A removable photothermal antibacterial "warm paste" target for cariogenic bacteria. Chem. Eng. J. **429**, 132491 (2022). https://doi.org/10.1016/j.cej.2021.132491
133. S.Y. Wang, B.H. Chen, L.P. Ouyang, D.H. Wang, J. Tan et al., A novel stimuli-responsive injectable antibacterial hydrogel to achieve synergetic photothermal/gene-targeted therapy towards uveal melanoma. Adv. Sci. **8**(18), 2004721 (2021). https://doi.org/10.1002/advs.202004721
134. D. Han, Y. Han, J. Li, X. Liu, K.W.K. Yeung et al., Enhanced photocatalytic activity and photothermal effects of cu-doped metal-organic frameworks for rapid treatment of bacteria-infected wounds. Appl. Catal. B **261**, 118248 (2020). https://doi.org/10.1016/j.apcatb.2019.118248
135. Q. Jia, Q. Song, P. Li, W. Huang, Rejuvenated photodynamic therapy for bacterial infections. Adv. Healthc. Mater. **8**(14), 1900608 (2019). https://doi.org/10.1002/adhm.201900608
136. Q. Zheng, X. Liu, Y. Zheng, K.W.K. Yeung, Z. Cui et al., The recent progress on metal-organic frameworks for phototherapy. Chem. Soc. Rev. **50**(8), 5086–5125 (2021). https://doi.org/10.1039/d1cs00056j
137. E.H. Morales, C.A. Pinto, R. Luraschi, C.M. Munoz-Villagran, F.A. Cornejo et al., Accumulation of heme biosynthetic intermediates contributes to the antibacterial action of the metalloid tellurite. Nat. Commun. **8**, 15320 (2017). https://doi.org/10.1038/ncomms15320
138. W. Wu, D. Mao, F. Hu, S. Xu, C. Chen et al., A highly efficient and photostable photosensitizer with near-infrared aggregation-induced emission for image-guided photodynamic anticancer therapy. Adv. Mater. **29**(33), 1700548 (2017). https://doi.org/10.1002/adma.201700548
139. Q. Li, W. Wang, H. Feng, L. Cao, H. Wang et al., NIR-triggered photocatalytic and photothermal performance for sterilization based on copper sulfide nanoparticles anchored on $Ti_3C_2T_x$ MXene. J. Colloid Interface Sci. **604**, 810–822 (2021). https://doi.org/10.1016/j.jcis.2021.07.048
140. K. Rajavel, S. Shen, T. Ke, D. Lin, Photocatalytic and bactericidal properties of MXene-derived graphitic carbon-supported TiO_2 nanoparticles. Appl. Surf. Sci. **538**, 148083 (2021). https://doi.org/10.1016/j.apsusc.2020.148083
141. B. Yan, X. Bao, X. Liao, P. Wang, M. Zhou et al., Sensitive micro-breathing sensing and highly-effective photothermal antibacterial cinnamomum camphora bark micro-structural cotton fabric via electrostatic self-assembly of MXene/HACC. ACS Appl. Mater. Interfaces **14**(1), 2132–2145 (2021). https://doi.org/10.1021/acsami.1c22740
142. S. Zada, H. Lu, F. Yang, Y. Zhang, Y. Cheng et al., V_2C nanosheets as dual-functional antibacterial agents. ACS Appl.

Bio Mater. **4**(5), 4215–4223 (2021). https://doi.org/10.1021/acsabm.1c00008

143. X. Nie, S. Wu, F. Huang, W. Li, H. Qiao et al., "Dew-of-Leaf" structure multiple synergetic antimicrobial modality hybrid: a rapid and long lasting bactericidal material. Chem. Eng. J. (2021). https://doi.org/10.1016/j.cej.2021.129072
144. W. Wang, H. Feng, J. Liu, M. Zhang, S. Liu et al., A photo catalyst of cuprous oxide anchored MXene nanosheet for dramatic enhancement of synergistic antibacterial ability. Chem. Eng. J. (2020). https://doi.org/10.1016/j.cej.2020.124116
145. S. Lv, B. Song, F. Han, Z. Li, B. Fan et al., MXene-based hybrid system exhibits excellent synergistic antibiosis. Nanotechnology **33**(8), 085101 (2022). https://doi.org/10.1088/1361-6528/ac385d
146. Q. He, H. Hu, J. Han, Z. Zhao, Double transition-metal TiVCT$_X$ MXene with dual-functional antibacterial capability. Mater. Lett. **308**, 131100 (2022). https://doi.org/10.1016/j.matlet.2021.131100
147. J. He, M. Shi, Y. Liang, B. Guo, Conductive adhesive self-healing nanocomposite hydrogel wound dressing for photothermal therapy of infected full-thickness skin wounds. Chem. Eng. J. **394**, 124888 (2020). https://doi.org/10.1016/j.cej.2020.124888
148. Y. Li, M. Han, Y. Cai, B. Jiang, Y. Zhang et al., Muscle-inspired MXene/PVA hydrogel with high toughness and photothermal therapy for promoting bacteria-infected wound healing. Biomater. Sci. **10**(4), 1068–1082 (2021). https://doi.org/10.1039/d1bm01604k
149. Z. Yang, X. Fu, D. Ma, Y. Wang, L. Peng et al., Growth factor-decorated Ti_3C_2 MXene/MoS_2 2D bio-heterojunctions with quad-channel photonic disinfection for effective regeneration of bacteria-invaded cutaneous tissue. Small **17**(50), 2103993 (2021). https://doi.org/10.1002/smll.202103993
150. C. Yang, Y. Luo, H. Lin, M. Ge, J. Shi et al., Niobium carbide MXene augmented medical implant elicits bacterial infection elimination and tissue regeneration. ACS Nano **15**(1), 1086–1099 (2021). https://doi.org/10.1021/acsnano.0c08045
151. X. Wang, M. Yao, L. Ma, P. Yu, T. Lu et al., NIR-responsive Ti_3C_2 MXene colloidal solution for curing purulent subcutaneous infection through the "nanothermal blade" effect. Adv. Healthc. Mater. **10**(14), 2100392 (2021). https://doi.org/10.1002/adhm.202100392
152. X. Zha, X. Zhao, J. Pu, L. Tang, K. Ke et al., Flexible anti-biofouling MXene/cellulose fibrous membrane for sustainable solar-driven water purification. ACS Appl. Mater. Interfaces **11**(40), 36589–36597 (2019). https://doi.org/10.1021/acsami.9b10606
153. I. Mahar, F.H. Memon, J.W. Lee, K.H. Kim, R. Ahmed et al., Two-dimensional transition metal carbides and nitrides (MXenes) for water purification and antibacterial applications. Membranes **11**(11), 869 (2021). https://doi.org/10.3390/membranes11110869
154. Z.W. Lei, X.T. Sun, S.F. Zhu, K. Dong, X.Q. Liu et al., Nature inspired MXene-decorated 3D honeycomb-fabric architectures toward efficient water desalination and salt harvesting. Nano-Micro Lett. **14**, 10 (2022). https://doi.org/10.1007/s40820-021-00748-7
155. H. Guan, T. Fan, H. Bai, Y. Su, Z. Liu et al., A waste biomass-derived photothermic material with high salt-resistance for efficient solar evaporation. Carbon **188**, 265–275 (2022). https://doi.org/10.1016/j.carbon.2021.12.029
156. Y. Li, T. Wu, H. Shen, S. Yang, Y. Qin et al., Flexible MXene-based Janus porous fibrous membranes for sustainable solar-driven desalination and emulsions separation. J. Cleaner Produc. **347**, 131324 (2022). https://doi.org/10.1016/j.jclepro.2022.131324
157. X. Nie, S. Wu, F. Huang, Q. Wang, Q. Wei, Smart textiles with self-disinfection and photothermochromic effects. ACS Appl. Mater. Interfaces **13**(2), 2245–2255 (2021). https://doi.org/10.1021/acsami.0c18474
158. L. Liu, W. Chen, H. Zhang, Q. Wang, F. Guan et al., Flexible and multifunctional silk textiles with biomimetic leaf-like MXene/silver nanowire nanostructures for electromagnetic interference shielding, humidity monitoring, and self-derived hydrophobicity. Adv. Funct. Mater. **29**(44), 1905197 (2019). https://doi.org/10.1002/adfm.201905197
159. S. Zhang, J. Ye, X. Liu, Y. Wang, C. Li et al., Titanium carbide/zeolite imidazole framework-8/polylactic acid electrospun membrane for near-infrared regulated photothermal/photodynamic therapy of drug-resistant bacterial infections. J. Colloid Interface Sci. **599**, 390–403 (2021). https://doi.org/10.1016/j.jcis.2021.04.109
160. W. Zhai, Y. Cao, Y. Li, M. Zheng, Z. Wang, MoO_{3-x} QDs/MXene ($Ti_3C_2T_x$) self-assembled heterostructure for multifunctional application with antistatic, smoke suppression, and antibacterial on polyester fabric. J. Mater. Sci. **57**(4), 2597–2609 (2022). https://doi.org/10.1007/s10853-021-06690-8